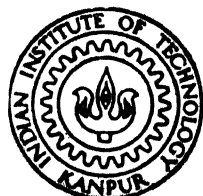


TEMPERATURE ANALYSIS OF ACCELERATED CUTTING : FINITE ELEMENT APPROACH

by

GAJENDRA KUMAR ADIL

ME
1987
M
ADI
TEM



DEPARTMENT OF MECHANICAL ENGINEERING

INDIAN INSTITUTE OF TECHNOLOGY, KANPUR

MARCH, 1987

TEMPERATURE ANALYSIS OF ACCELERATED CUTTING : FINITE ELEMENT APPROACH

A Thesis Submitted
In Partial Fulfilment of the Requirements
for the Degree of
MASTER OF TECHNOLOGY

by
GAJENDRA KUMAR ADIL

to the
DEPARTMENT OF MECHANICAL ENGINEERING
INDIAN INSTITUTE OF TECHNOLOGY, KANPUR
MARCH, 1987

ENTRANCE INDEX

No. A 8888

ME-1987-M-ADI-TEM

Dedicated

To

My Parents

CERTIFICATE

3/3/87

This is to certify that this work entitled,
"TEMPERATURE ANALYSIS OF ACCELERATED CUTTING : FINITE
ELEMENT APPROACH" by Gajendra Kumar Adil has been
carried out under our supervision and it has not been
submitted elsewhere for a degree.



(Dr. T. Sundararajan)
Assistant Professor
Dept. of Mechanical Engg.
I.I.T. Kanpur



(Dr. V.K. Jain)
Assistant Professor
Dept. of Mechanical Engg.
I.I.T. Kanpur

March 3, 1987.

ACKNOWLEDGEMENTS

I express my deep sense of gratitude and appreciation to my thesis supervisors Dr. V.K. Jain and Dr. T. Sundararajan for their inspiring guidance, valuable suggestions, constructive criticisms and constant encouragement throughout the present work.

I am thankful to my friends Bharat, Sanjeev, Rekhu for their help and encouragement during various stages.

Last but not the least thanks are due to Mr. U.S. Mishra for his excellent typing and Mr. B.K. Jain for making tracings.

March, 1987.

-GAJENDRA KUMAR ADIL

CONTENTS

LIST OF TABLES
 LIST OF FIGURES
 NOMENCLATURE
 ABSTRACT

	<u>Page</u>	
Chapter 1	INTRODUCTION AND LITERATURE SURVEY	1
	1.1 Introduction	1
	1.2 Review of Previous Work	3
	1.3 Objectives of Present Work	7
CHAPTER 2	THEORETICAL ANALYSIS	9
	2.1 Shear Angle, Shear and Frictional Force and Shear Flow Stress	9
	2.2 Shear Strain, Strain Rate	11
	2.3 Shear Strain Acceleration during Taper Turning and Facing Operations	14
CHAPTER 3	CO-ORDINATE, VELOCITY AND HEAT GENERATION	20
	3.1 Dimensionless Co-ordinates	20
	3.2 Estimation of Machining Zone Dimensions	26
	3.3 Velocity Field	28
	3.3 (a) For Uncut Metal and Chip	28
	3.3 (b) Primary Shear Deformation Zone (PSDZ)	28
	3.3 (c) In Secondary Plastic Zone	33
	3.4 Calculation of Heat Generation	33
CHAPTER 4	FINITE ELEMENT ANALYSIS	35
	INTRODUCTION	35
	4.1 Description of FE Technique	35
	4.2 Shape Functions and Their Local Derivatives	46
	4.3 Global Derivatives and Numerical Integration	49
	4.3 (a) Global Derivatives	49
	4.3 (b) Numerical Integration	50
	4.4 Evaluation of Boundary Integrals	51
	4.5 Solution of Simultaneous Linear Differential Equations	52
	4.6 Average Temperature Along Tool-Chip Interface	54

	<u>Page</u>
CHAPTER 5 RESULTS AND DISCUSSION	55
5.1.1 Comparison of Present Model with Other Analytical Model	55
5.1.2 Comparison with Experimental Results	57
5.2 Temperature Distribution	60
5.3 Parametric Study in Longitudinal Turning and Accelerated Cutting	66
CHAPTER 6 CONCLUSIONS AND SUGGESTIONS FOR FUTURE WORK	
6.1 Conclusions	72
6.2 Suggestions For Future Work	73
REFERENCES	75
APPENDICES	
APPENDIX I. Experimental Data	77
Levels for Different Factors (Table A1-A3)	79
Plan of Experiment (Table A4-A6)	82
Constants of Response Surface Model (Table A-7)	86
Temperature Calibration Chart	87
APPENDIX II. Physical and Machining Constants	88
Table (A8-A9)	

LIST OF TABLES

<u>Table</u>	<u>Title</u>	<u>Page</u>
2.1	Constants for Calculation of ϕ in the Expression of form $\phi = AN^{n_{11}} \theta_t^{n_{12}} f^{n_{13}} V^{n_{14}}$	16
3.1	Geometric Parameters of Different Zones	24
5.1	Comparison of Maximum Temperatures obtained Using Present Model and Other Analytical Model during Longitudinal Turning	56

LEVELS FOR DIFFERENT FACTORS

A1	Longitudinal Turning	79
A2	Taper Turning	80
A3	Facing	81

PLAN OF EXPERIMENTS

A4	Longitudinal Turning	82
A5	Taper Turning	83
A6	Facing	85
A7	Values of Constants in Response Surface Model (Eqn. A1.1) For Average Tool-Chip Interface Temperature	86
A8	Physical Properties of Tool Work Materials Used	88
A9	Constants of Power Law equation in the for $B = A N^{n_{11}} \theta_t^{n_{12}} f^{n_{13}} V^{m_{14}}$	88

LIST OF FIGURES

<u>FIGURE</u>	<u>TITLE</u>	<u>PAGE</u>
1.1	Assumed Deformation Zone Shape	5
2.1	Chip Formation and Deformation during Orthogonal Cutting	10
2.2	Merchant's Force Circle Diagram	10
2.3		10
2.4	Concept of Shear Strain	12
2.5	Elements of Chip in Strained Shape	12
2.6	Enlarged View of Area ABC of Fig. 2.5	12
2.7	Taper Turning	15
2.8	Facing	15
3.1	Parallelogram Shaped Zone ABCD	22
3.2	Division of Solution Domain (Twelve Zones)	22
3.3(a)	Force Diagram	27
3.3(b)	Hyperbolic Model of Streamline	27
3.4	Velocity Diagram	27
3.5		27
4.1	Finite Element Mesh	42
4.2	Problem Region, Showing the Thermal Boundary Conditions	43
4.3	Finite Element in (a) x-y Domain (b) r-s domain	43
4.4	A typical Boundary (Line) Element	43

<u>FIGURE</u>	<u>TITLE</u>	<u>PAGE</u>
5.1	Comparison of Analytical and Experimental Average Temperatures (a) Longitudinal Turning (b) Facing	59
5.2(a)	Temperature Distribution in Taper Turning	61
5.2(b)	Temperature Distribution in Facing	62
5.3	Temperature Distribution in Longitudinal Turning	63
5.4	Variation of Temperature on Rack Face and Flank Face of Tool	65
*		
5.6(a)	Cutting Speed vs. Thermo e.m.f. [Ref. 12]	70
5.6(b)	Variation of Thermo e.m.f. (temperature) during Longitudinal Turning and Taper Turning [Ref. 20].	71
* 5.5 (a-d)	Comparison of average tool-chip interface temperature during longitudinal turning, taper turning and facing.	68-69

NOMENCLATURE

C_S	side tool clearance angle
C_P	specific heat at constant pressure
D_A	bigger end diameter of a tapered job
D_B	smaller end diameter of a tapered job
DS	mean width of primary shear deformation zone (PSDZ)
d	depth of cut (tool width)
F_c	cutting force
F_f	frictional force along the rake face
F_N	component of force normal to rake face
F_R	resultant force
F_S	shear force
F_{sn}	component of force normal to the shear plane
F_t	thrust force
f	uncut chip thickness (feed rate)
H	chip contact length
h	convective heat transfer coefficient
k	thermal conductivity
l	length of primary shear deformation zone (PSDZ) along shear plane
N	revolutions per minute
\dot{Q}	heat generation rate (per unit volume)
\dot{Q}_{SZintp}	heat generation rate/volume in tool-chip interface due to secondary plastic deformation
$\Delta \dot{Q}_{SZF}$	heat generation rate/volume in secondary zone due to friction

r	chip thickness ratio
$T_{av.}$	average tool-chip interface temperature
t	machining time
t_c	deformed chip thickness
u	x-component of velocity
v	cutting speed
v_c	fully developed chip velocity
v_{int}	tool-chip interfacial velocity
v_s	shear velocity
v	y-component of velocity
x	co-ordinate along a direction opposite to cutting direction
y	co-ordinate along a direction normal to x-direction

GREEK LETTERS

α	rake angle
δt_2	maximum thickness of secondary zone
θ_t	semi-taper angle
λ	frictional angle
μ	coefficient of friction
$\dot{\nu}$	streak rate
$\ddot{\nu}$	strain acceleration
ρ	density
τ	shear stress
ϕ	shear angle

ACRONYMS

BUE	built-up-edge
PSDZ	primary shear deformation zone.

ABSTRACT

It has been reported by different researchers that shear strain acceleration governs the machining parameters like, microhardness of chips, shear angle, tool wear, tool-chip interface temperature etc. Experimental and analytical studies have been made about dependence of tool-chip interface temperature on machining parameters during longitudinal turning. Experimental findings for above have also been reported during accelerated cutting. However, no literature is available to predict temperature during accelerated cutting (viz. facing and taper turning) analytically.

In present work a general purpose finite element method (FEM) programme has been developed to calculate the average tool-chip interface temperature and temperature distribution in the tool-chip-work system during longitudinal turning as well as accelerated cutting. Suitable models for velocity field and heat generation in different zones have been used.

The analytical (FEM) results have been compared against experimental and analytical results of other researchers. A comparison of tool-chip interface temperature in accelerated cutting has been made with that in longitudinal turning to investigate the effect of shear strain acceleration on temperature attained during accelerated machining.

It has been concluded that the average tool-chip interface temperature is highest in case of longitudinal turning and lowest in the case of facing. It is also observed that the temperature distribution pattern in all the three cases is approximately the same, except their magnitude.

CHAPTER 1

INTRODUCTION AND LITERATURE SURVEY

1.1 INTRODUCTION:

One of the most important aspects of today's metal cutting research is how to increase the productivity. The productivity itself is related to the life of cutting tool. Further, commonly used criteria for the evaluation of ease or difficulty with which any material can be machined (i.e. machinability) is tool life. Thus, to a certain extent, machinability evaluation helps in yielding higher productivity and developing new tool materials. Longitudinal turning is commonly used method for machinability evaluation. But, it suffers from inherent disadvantages of being slow, large amount of material consuming and expensive. Therefore, accelerated cutting tests viz. facing [1] and taper turning [2] were proposed for quick evaluation of the machinability. But, Jain and Pandey [3] reported that accelerated machinability test-results should be used with caution as they will be reliable only when shear strain acceleration is kept below a certain critical value, inspite of theoretical backing for these tests.

The temperature attained during machining operation affects the properties of both, tool and work materials. In

other words, temperature is a critical factor which influences the shear angle, micro-hardness of chips, cutting forces, tool wear, surface finish etc.

The following experimental techniques have been commonly used for evaluation of mean tool-chip interface temperature and temperature distributions in tool, chip and work surface [4].

1. Tool-work thermocouple,
2. Radiation pyrometer,
3. Colour paints.

There are no simple and reliable experimental methods for determining the temperature field in the tool, chip and workpiece, even for the simple case of steady state orthogonal cutting. Therefore, analytical approaches although quite complicated, are relied on to make indepth analysis of thermal aspects of metal cutting process.

Because of the high speed computation capabilities of moden age computers, numerical techniques like finite element methods (FEM) and finite difference methods (FDM) are being used to analyse the temperature field in machining. There are advantages of using FEM over FDM, such as a general purpose computer programme can be developed for a complex and changing geometry problems like the one encountered in metal cutting situation. By changing the input data only, it is possible to analyse the varieties of problems with different geometries and boundary conditions. It is not possible in case of FDM.

1.2 REVIEW OF PREVIOUS WORK:

Several investigators have studied, theoretically and experimentally, the temperature variation during orthogonal longitudinal turning. The average temperature rise in the cutting zone has been theoretically estimated by Zorev [5]. Reported estimation was based on the assumption that the total heat generated is distributed among the tool, chip and work-piece. Later on, theoretical analyses were also done by Weiner [6] and Rapier [7].

Finite element method (FEM) to determine the temperature around the cutting edge was first applied by Tay et al [8]. The concept of hyperbolic streamlines for obtaining the velocity fields and the strain rates in the primary shear deformation zone was used. Semi-empirical models have been used for calculating the heat generation in the primary and secondary zone. The FE solution was based on the variational formulation and quadrilateral elements were used for discretizing the solution domain consisting of a part of tool, chip and work material.

Murarka et al [9] obtained the average chip-tool interface temperature using the Galerkin's approach of the finite element method for a wide range of cutting conditions. In his model, the shear strain-rate and velocity distributions in the primary and secondary deformation zones were determined experimentally using a grid technique. Empirical expressions for the flow stress, in the primary zone, in terms of the strain, strain-rate and temperature were used. Heat generated

at the interface of flank face and machined work surface was also accounted.

Modifications in the model of Tay et al [8] were made by Stevenson et al [10]. The FE programme developed in the earlier work for calculating the temperature distributions in the chip and tool were extended in its range of application. Specifically, the programme no longer needed a flow field as input and it could accommodate a wide range of shear angle and contact lengths. The finite element temperature field results were compared with temperatures obtained using metallographic method.

Balaji [11] measured average tool-chip interface temperature while machining mild steel work using, both coated and uncoated WC tools. Using FEM, he computed average tool-chip interface temperature and temperature field in tool, chip and work material. He compared analytical results with his own experimental results. Simple linear model for velocity variation in the primary and secondary zone was assumed.

Velocity components (Fig. 1.1) u (along x direction) and v (along y-direction) were calculated as

In the zone I_a ,

$$u = \frac{2V + V_c \sin\alpha}{3}$$

$$v = \frac{V_c \cos\alpha}{3}$$

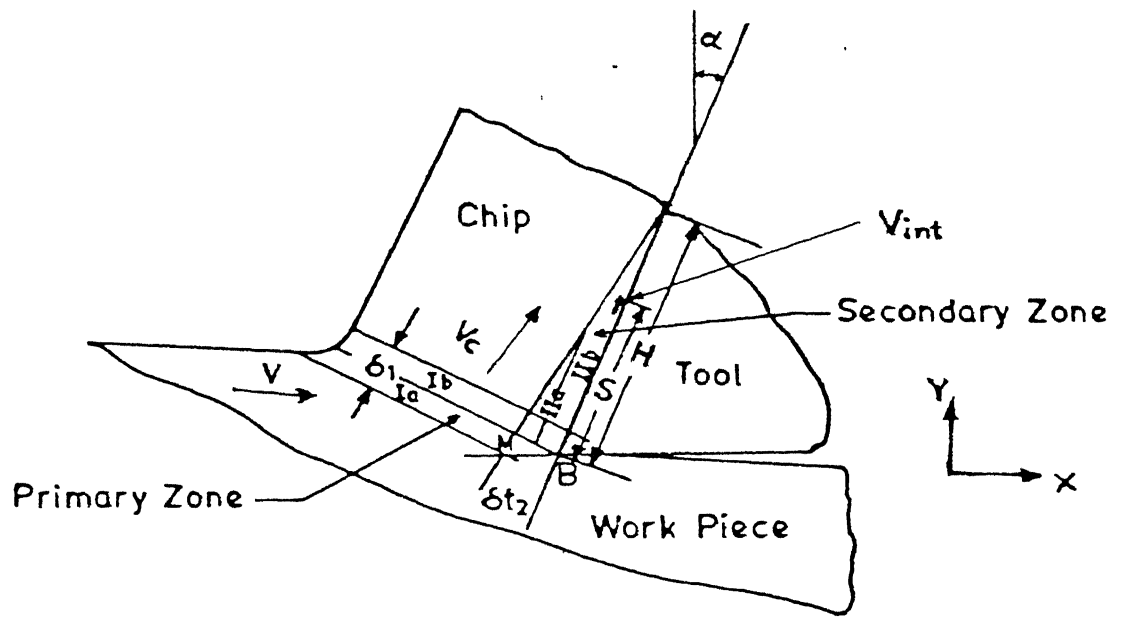


Fig. 1.1 Assumed deformation zone shape.

In zone I_b,

$$u = \frac{V + 2V_c \sin \alpha}{3}$$

$$v = \frac{2V_c \cos \alpha}{3}$$

In zone II_a,

$$u = (2V_c + V_{int}) \frac{\sin \alpha}{3}$$

$$v = (V_c + V_{int}) \frac{\cos \alpha}{3}$$

and In zone II_b,

$$u = (V_c + 2V_{int}) \frac{\sin \alpha}{3}$$

$$v = (V_c + 2V_{int}) \frac{\cos \alpha}{3}$$

where,

$$V_{int} = \frac{1}{3} V_c \sqrt{1 + 8 \frac{S}{H}} .$$

The three noded triangular elements were used as discriminating elements.

The first attempt for measuring temperature during accelerated machining was made by Jain [12]. He measured tool-chip interface temperature (mV recording of thermo e.m.f.) during facing test, using H.S.S. tool and mild-steel as a work material. Jain and Pandey [13] determined temperature experimentally for facing as well as taper turning, using cast iron

as work material and H.S.S. as tool material. It was concluded that strain acceleration plays an important role and it governs different parameters during accelerated cutting. Instantaneous temperature values obtained during facing and longitudinal turning for the same cutting conditions were found to be different. They concluded that accelerated tests for machinability evaluation are not reliable methods unless they are performed within the prescribed shear strain acceleration conditions.

1.3 OBJECTIVES OF PRESENT WORK:

From the above literature survey, it is evident that no analytical work has been reported for temperature evaluation during accelerated cutting. Keeping this in view, finite element technique has been used to estimate the temperature distributions in the tool, chip and workpiece, during accelerated as well as longitudinal cutting situations. Temperature is also presented in the form of average tool-chip interface temperature for a range of cutting conditions.

In the present model, suitable approximations for velocity field and heat generations in different zones have been proposed. By making an energy balance and assuming two dimensional heat transfer situation, the problem is analyzed using a general purpose finite element programme.

The validity of the analytical model has been tested by comparing the analytical results with those obtained

experimentally by Jain [12] during facing and longitudinal turning. Finally, the effects of shear strain acceleration on temperature are investigated by comparing accelerated cutting results with those of conventional turning.

CHAPTER 2

THEORETICAL ANALYSIS

Elaborate studies have been made in the field of mechanics of orthogonal metal cutting. Here, theoretical analysis for the case of accelerated cutting, viz. taper turning and facing operations, in which cutting speed varies continuously during the cut, has also been included.

2.1 SHEAR ANGLE, SHEAR AND FRICTIONAL FORCE AND SHEAR FLOW STRESS:

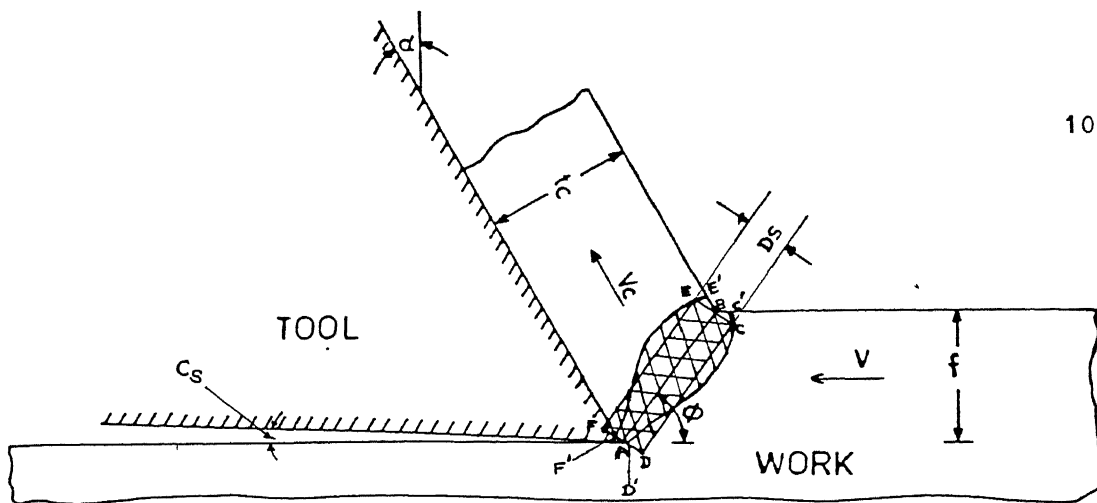
In an attempt to study stress-strain properties during machining process, Kececioglu [14] obtained photomicrographs of the plastic zone, using quick stop device (QSD). Based on these photomicrographs, he assumed that plastic zone could be represented by a parallel sided shear zone, similar to that shown in Fig. (2.1).

The line AB is the centre line of actual shear zone DCEF and known as shear plane (Fig. 2.1). The position of shear plane is defined by ϕ , known as the shear angle and it can be evaluated (Fig. 2.3), from the equation (2.1) as

$$\tan \phi = \frac{r \cos \alpha}{1 - r \sin \alpha} \quad (2.1)$$

where,

r is chip thickness ratio given by,



AREA D'C'E'F' Plastic deformation zone obtained from photomicrographs.

AREA DCEF Approximation of D'C'E'F' in to a parallel sided zone.

Fig. 2.1 Chip formation and deformation during orthogonal cutting

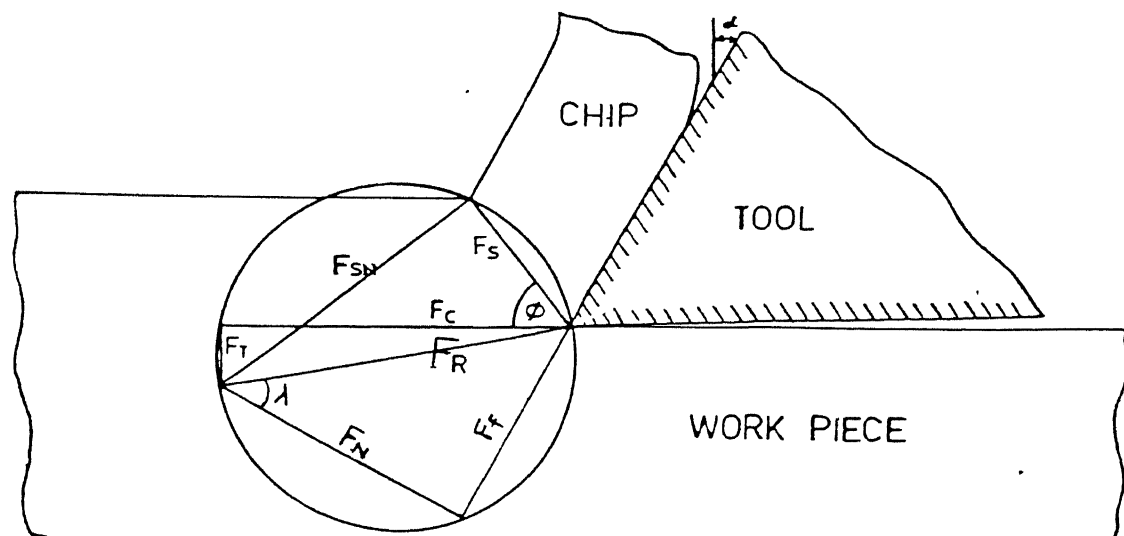


Fig. 2.2 Merchant's force circle diagram.

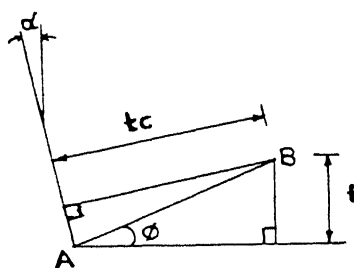


Fig 2.3

$$r = \frac{f}{t_c} = \frac{l_2}{l_1} \quad (2.2)$$

where,

l_1 and l_2 are lengths of undeformed and deformed chip respectively

f = feed rate (undeformed chip thickness)

t_c = deformed chip thickness.

Forces can be evaluated using Ernest and Merchant's model of thin shear zone [15]. Merchant's force circle diagram is shown in the Fig. (2.2).

Mean shear stress, τ , is given by

$$\tau = \frac{(F_c \cos \phi - F_t \sin \phi) \sin \phi}{f \cdot d} \quad (2.3)$$

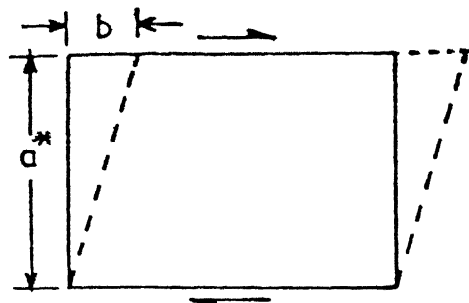
where,

d = depth of cut.

2.2 SHEAR STRAIN, STRAIN RATE:

Shear strain is defined as the deformation per unit length, i.e. if a rectangular block of height 'a' slips by an amount 'b' (Fig. 2.4) then, strain,

$$\gamma = \frac{b}{a} \quad (2.4)$$



12

Fig. 2.4 Concept of shear strain

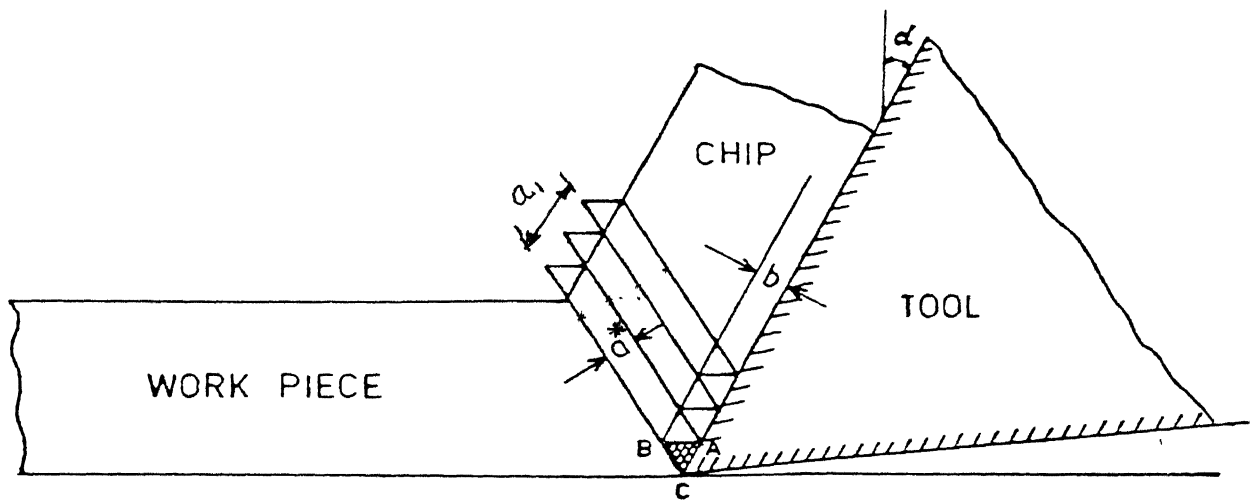


Fig. 2.5 Elements of chip in strained state.

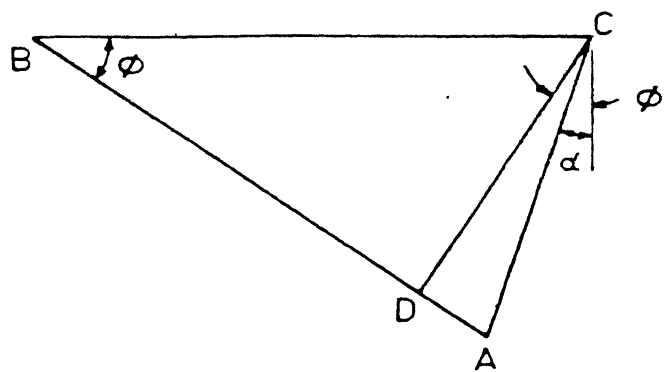


Fig. 2.6 Enlarged view of area ABC of fig. 2.5

The chips can be considered as composed of a large number of elements of thickness 'a' and then each element suffers a displacement 'b' after crossing the shear zone, Fig.(2.5). Then, it is clear from Fig. (2.6) that

$$= \frac{\cos \alpha}{\sin \phi \cdot \cos(\phi - \alpha)} \quad (2.5)$$

If 'dt' is the time taken by the metal to move through a distance '2a' in PSDZ and V is cutting speed, then strain rate

$$\dot{\nu} = \frac{d\nu}{dt} \quad (2.6)$$

$$= \frac{V \cos \alpha}{2a \cos(\phi - \alpha)} \quad (2.7)$$

where,

$$2a_1 = \text{thickness of PSDZ} = DS .$$

Hence,

$$\dot{\nu} = \frac{V \cos \alpha}{DS \cdot \cos(\phi - \alpha)} \quad (2.8)$$

Jain and Pandey [16] have shown analytically that the mean width of PSDZ can be given by

$$DS = \frac{\sqrt{2} f \sin(90 + \alpha - \phi)}{4 \sin \phi \cdot \sin(45 - \alpha + \phi)} \quad (2.9)$$

2.3 SHEAR STRAIN ACCELERATION DURING TAPER TURNING AND FACING OPERATIONS:

During taper turning, cutting speed increases, as cut proceeds from smaller end towards larger end, as shown in Fig. (2.7). The speed at any instant 't' is given by

$$V_t = \frac{\pi N}{1000} [D_B + 2 \tan \theta_t \cdot Nft] \quad (2.10)$$

For facing, the cutting speed at any time 't' after the cutting starts at inner dia D_i Fig.(2.8), can be written as

$$V_f = \frac{\pi N}{1000} [D_i + 2Nft] \quad (2.11)$$

If the variations in ' ϕ ' for taper turning and facing can be represented in the following forms, assuming constant depth of cut, then

$$\phi_t = A_1 N^{n_{11}} \cdot \theta_t^{n_{12}} \cdot f^{n_{13}} \cdot V_t^{n_{14}} \quad (2.12)$$

$$\phi_f = B_1 N^{m_{11}} \cdot f^{m_{13}} \cdot V_f^{m_{14}} \quad (2.13)$$

where the constants A_1 , n_{11} , n_{12} , n_{13} , n_{14} , B_1 , m_{11} , m_{13} , m_{14} can be found experimentally. A typical set of values of these constants are given in Table (2.1).

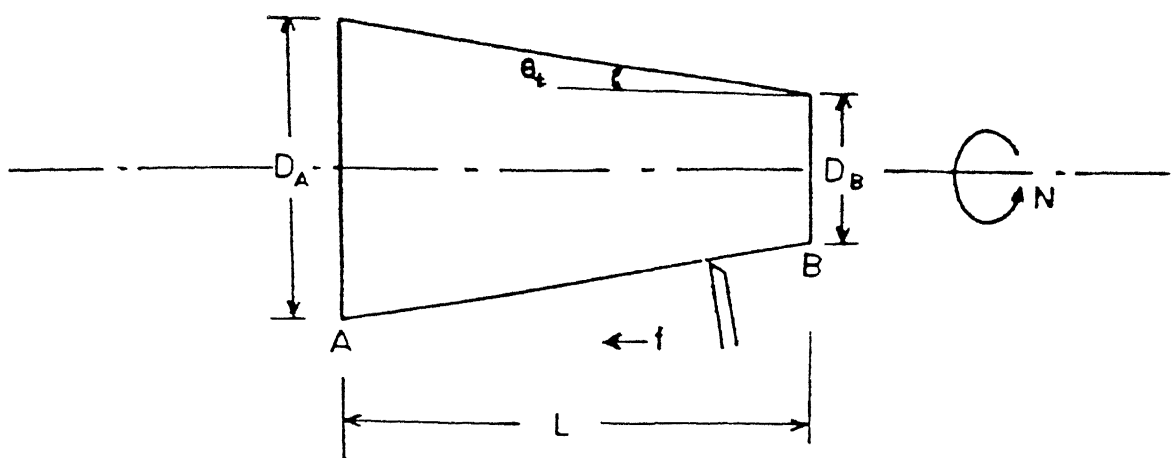


Fig. 2.7 Taper turning

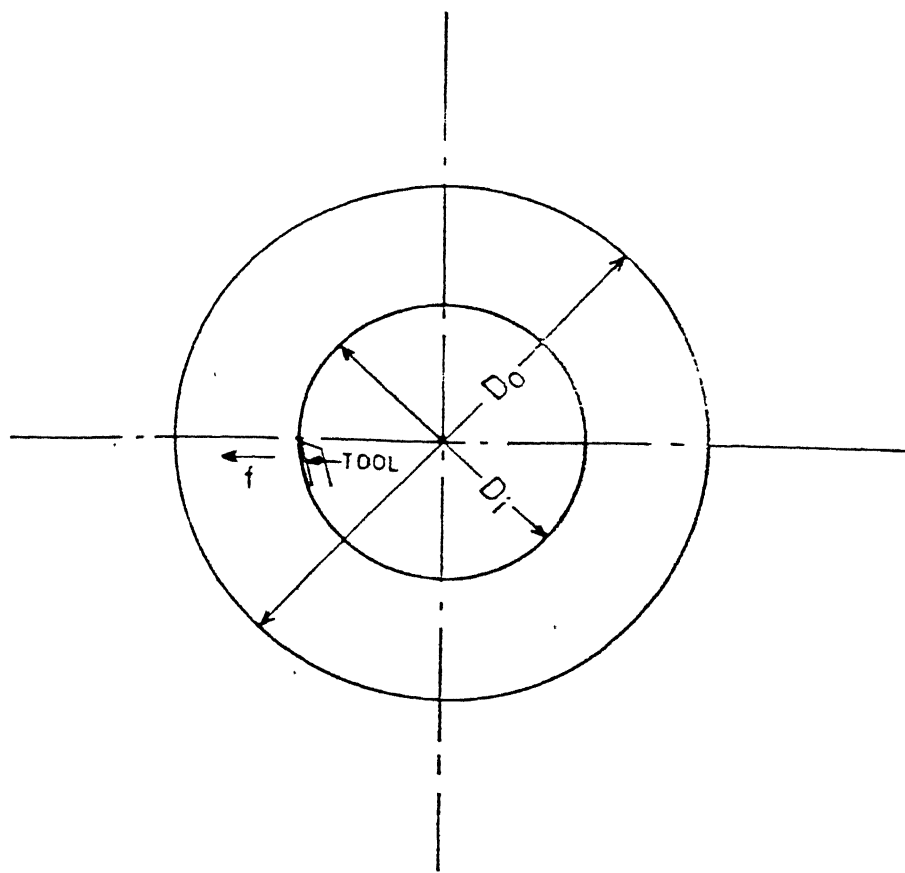


Fig. 2.8 Facing

TABLE 2.1 : Constants Used For Calculation of \emptyset in the expression of form, $\emptyset = A N^{n_{11}} \theta_t^{n_{12}} f^{n_{13}} V^{n_{14}}$ (Using results from Ref. [7])

Taper Turning	Facing
$A = 30.5395$	$B = 82.2896$
$n_{11} = 0.0141$	$m_{11} = -0.1729$
$n_{12} = 0.056$	$m_{12} = 0.0000$
$n_{13} = 0.2352$	$m_{13} = 0.0626$
$n_{14} = -0.1418$	$m_{14} = 0.1404$

When cut proceeds, all quantities in R.H.S. of eqns. (2.12 and 2.13) except 'V' remain same, so one can write the above equations in the form

$$\emptyset = A_{\emptyset} V^n \quad (2.14)$$

where,

A_{\emptyset} is a constant given by

$$A_{\emptyset} = A_1 \cdot N^{n_{11}} \cdot \theta_t^{n_{12}} \cdot f^{n_{13}} \quad (2.15)$$

(for taper turning)

and,

$$A_{\phi} = B_1 \cdot N^{m_{11}} \cdot f^{m_{13}} \quad (2.16)$$

(for facing)

$$V^n = V_t^{n_{14}} \quad (2.17)$$

(for taper turning)

$$V^n = V_f^{m_{14}} \quad (2.18)$$

(for facing)

Strain rate from eqns. (2.8) and (2.9) becomes

$$\dot{\nu} = \frac{4V \cos \alpha \cdot \sin \phi \cdot \sin(45 + \phi - \alpha)}{\sqrt{2} \cos^2(\phi - \alpha)} \quad (2.19)$$

Strain acceleration is given by,

$$\ddot{\nu} = \frac{d\dot{\nu}}{dt} \quad (2.20)$$

Differentiating (2.19) logarithmically with respect to 't', we have

$$\frac{\ddot{\nu}}{\dot{\nu}} = 0 + \frac{\dot{V}}{V} + \frac{\cos \phi}{\sin \phi} \cdot \dot{\phi} + \frac{\cos(45 + \phi - \alpha)}{\sin(45 + \phi - \alpha)} \cdot \dot{\phi} - 2 \left\{ \frac{\sin(\phi - \alpha)}{\cos(\phi - \alpha)} \right\} \dot{\phi} \quad (2.21)$$

where,

$$\dot{V} = \frac{dV}{dt} \quad (2.22)$$

$$\dot{\phi} = \frac{d\phi}{dt} \quad (2.23)$$

Differentiating (2.14) w.r.t. 't', we have

$$\dot{\phi} = \frac{\pi}{180} A_{\phi} \circ n V^{n-1} \dot{V} \quad (2.24)$$

$$= \frac{\pi}{180} n \dot{\phi} \circ \frac{\dot{V}}{V} \quad (2.25)$$

Since ϕ is in degree in eqn. (2.14).

From eqns. (2.21 - 2.25),

$$\ddot{\nu} = \dot{\nu} \frac{\dot{V}}{V} \left[1 + \frac{\pi}{180} \dot{\phi} n \{ \text{Cot } \phi + \text{Cot } (45 + \phi - \alpha) + 2 \tan(\phi - \alpha) \} \right] \quad (2.26)$$

Hence, strain acceleration for taper turning can be evaluated as,

$$\ddot{\nu}_t = \dot{\nu}_t \frac{\dot{V}_t}{V_t} \left[1 + \frac{\pi}{180} \dot{\phi}_t n_{14} \{ \text{Cot } \phi_t + \text{Cot}(45 + \phi_t - \alpha) + 2 \tan(\phi_t - \alpha) \} \right] \quad (2.27)$$

where,

\dot{V}_t can be found by differentiating (2.10) w.r.t. 't' and given as

$$\dot{V}_t = \frac{2\pi N^2 f}{1000} \tan \theta_t \quad (2.28)$$

and

$V_t, n_{14}, \phi_t, \dot{\nu}_t$ are given by eqns. (2.10, 2.12, 2.19).

Similarly, strain acceleration for facing is given by,

$$\ddot{\nu}_f = \frac{\dot{\nu}_f \dot{V}_f}{V_f} [1 + \frac{\pi}{180} \phi_f + m_{14} \{ \cot \phi_f + \cot(45 + \phi_f - \alpha) \\ + 2 \tan(\phi_f - \alpha) \}] \quad (2.29)$$

where,

$$\dot{V}_f = \frac{2\pi N_f^2}{1000} \quad (2.30)$$

(obtained from eqn. 2.11)

$\dot{V}_f, \phi_f, m_{14}, \dot{\nu}_f$ are given by eqns. (2.11, 2.13, 2.19).

In the work reported in this thesis, eqns. (2.10-2.13, 2.19, 2.27-2.29). have been used for computation purposes.

CHAPTER 3

CO-ORDINATE, VELOCITY FIELD AND HEAT GENERATION

3.1 DIMENSIONLESS CO-ORDINATES:

Unlike in longitudinal turning, cutting speed changes continuously in accelerated cutting as the cutting progresses with time. This change in cutting speed alters the values of different cutting parameters like shear angle, thickness of PSDZ, chip contact length, forces etc. [17,16,8]. Thus, in turn, the configuration of the solution domain changes with time (cutting speed), and co-ordinates of any point in the domain are functions of time. To take into account the grid size variation, the domain is divided into several zones Fig.(3.2), and the co-ordinates of a point in any of these zones are non-dimensionalized with respect to the two adjacent sides of a parallelogram, either made by the sides of that particular zone or by enlarged lines containing that zone sides. The co-ordinates in the non-dimensional form are kept the same with time, while the actual zone configuration and the orientation may change. The current configuration at any time 't' can be mapped into the initial configuration (at time $t=0$), by suitably transforming it through translation, rotation and scaling.

Thus, at any time a transformation matrix can be found which when multiplied with non-dimensional co-ordinates gives the co-ordinates of any point at that instant.

Mathematically speaking,

$$\{X_p(t)\} = [TR(t)] \{X_{pd}\} \quad (3.1)$$

where,

$\{X_p(t)\}$ = co-ordinates of a point at time 't'

$[TR(t)]$ = co-ordinate transformation matrix at time 't'

$\{X_{pd}\}$ = non-dimensional co-ordinates of point, given at time $t = 0$ (remains fixed).

Such a transformation for a parallelogram-shaped zone is shown in Fig. (3.1).

In the figure, ABCD is the zone configuration at any time 't'. It can be described by dimensions l_1 , l_2 and the angles, θ_1 , θ_2 . x_A and y_A are the co-ordinates of the corner point, A.

Let (x_p, y_p) be the physical co-ordinates of a point P, within the zone ABCD. In the transformed space, x_{pd} and y_{pd} are the dimensionless co-ordinates.

Then,

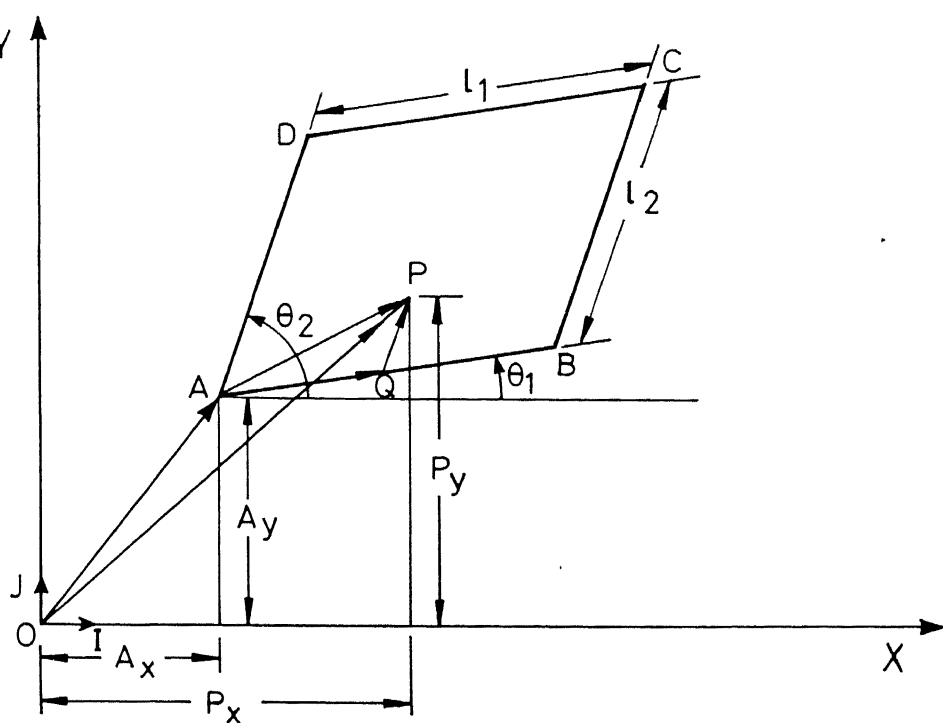


Fig. 3.1 Parallelogram shaped zone ABCD.

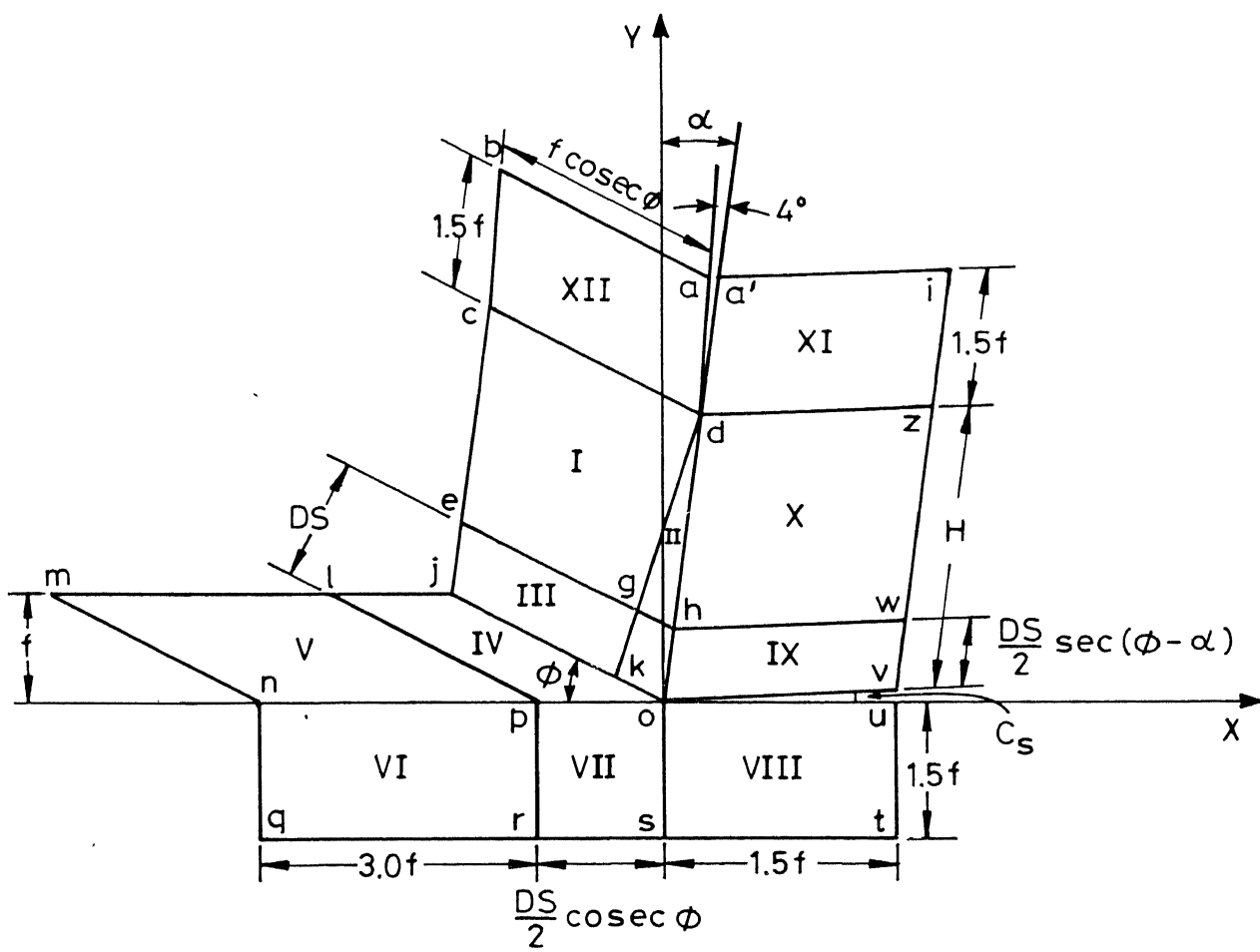


Fig. 3.2 Division of solution domain (twelve zones)

$$x_{Pd} = \frac{AQ}{l_1} \quad (3.2)$$

$$y_{Pd} = \frac{QP}{l_2} \quad (3.3)$$

$$\overrightarrow{OP} = (\overrightarrow{AQ} + \overrightarrow{QP}) + \overrightarrow{OA} \quad (3.4)$$

From eqns.(3.2-3.4) and Fig.(3.1),

$$\begin{aligned} x_{P^I} + y_{P^J} &= (x_{Pd} \cdot l_1 \cos \theta_1 + y_{Pd} l_2 \cos \theta_2 + A_x) I \\ &+ (x_{Pd} \cdot l_1 \sin \theta_1 + y_{Pd} l_2 \sin \theta_2 + A_y) J \end{aligned} \quad (3.4a)$$

Above equation can be written in the matrix form as

$$\begin{Bmatrix} x_P \\ y_P \\ 1 \end{Bmatrix} = \begin{bmatrix} l_1 \cos \theta_1 & l_2 \cos \theta_2 & A_x \\ l_1 \sin \theta_1 & l_2 \sin \theta_2 & A_y \\ 0 & 0 & 1 \end{bmatrix} \begin{Bmatrix} x_{Pd} \\ y_{Pd} \\ 1 \end{Bmatrix} \quad (3.5)$$

Figure (3.2) shows the geometry parameters of different zones. The parameters have also been tabulated in Table 3.1. These parameters have been used for calculating transformation matrix.

TABLE 3.1 : Geometric Parameters of Different Zones

ZONE No. ↓	GEOMETRY PARA- METER ↑	l_1	l_2	θ_1	θ_2	A_x	A_y
I hdce	$H - \frac{DS}{2} \sec(\phi - \alpha)$	$90 - \alpha$	$f \cosec \phi$	$180 - \phi$	$\frac{DS}{2} \sec(\phi - \alpha) \cdot \sin \alpha$	$\frac{DS}{2} \sec(\phi - \alpha) \cdot \cos \alpha$	
* II hdg	$H - \frac{DS}{2} \sec(d - \alpha)$	$90 - \alpha$	$f \cosec \phi$	$180 - \phi$	$\frac{DS}{2} \sec(\phi - \alpha) \sin \alpha$	$\frac{DS}{2} \sec(\phi - \alpha) \cos \alpha$	
III obj	$\frac{DS}{2} \sec(\phi - \alpha)$	$90 - \alpha$	$f \cosec \phi$	$180 - \phi$	0	0	
IV objp	$\frac{DS}{2} \cosec \phi$	180	$f \cosec \phi$	$180 - \phi$	0	0	
V plmn	3.0f	180	$f \cosec \phi$	$180 - \phi$	$-\frac{DS}{2} \cosec \phi$	0	
VI pnqr		180	1.5f	270	$-\frac{DS}{2} \cosec \phi$	0	
VII oprs	$\frac{DS}{2} \cosec \phi$	180	1.5f	270	0	0	

Continued.....

TABLE:3.1 (Continued):

ZONE No. +	GEOMETRY PARAMETER →	l_1	θ_1	l_2	θ_2	A_x	A_y
VIII ostu		1.5f	0.0	1.5f	270	0	0
IX ovwh		1.5f	c_s	$\frac{DS}{2} \text{Cosec}(\phi-\alpha)$	$90-\alpha$	0	0
X hwzd		$H - \frac{DS}{2} \cdot \text{Sec}(\phi-\alpha)$	$90-\alpha$	1.5f	c_s	$\frac{DS}{2} \cdot \text{Sec}(\phi-\alpha) \text{Sin}$	$\frac{DS}{2} \cdot \text{Sec}(\phi-\alpha) C_o$
XI dzia'		1.5f	$90-\alpha$	1.5f	c_s	$H \text{Sin} \alpha$	$H \text{Cos} \alpha$
XII dabc		1.5f	$90-\alpha+4$	$f \text{Cosec} \phi$	$180-\phi$	$H \text{Sin} \alpha$	$H \text{Cos} \alpha$

* Co-ordinates (dimensionless) for a point in zone II is given by non-dimensionalizing w.r.t. sides hd and he .

3.2 ESTIMATION OF MACHINING ZONE DIMENSIONS:

The length (l) of the primary shear deformation zone (PSDZ) along the shear plane is given by

$$l = f / \sin \theta \quad (3.6)$$

Secondary zone is assumed to be triangular in shape. The maximum thickness of secondary shear zone (δt_2) has been reported by Tay et al [8] as:

$$\delta t_2 = 0.05 t_c \quad (3.7)$$

In the present analysis, the secondary plastic zone is assumed to extend over the entire contact length, neglecting the elastic contact region which occurs just before the chip leaves the rake face. A good estimate of the chip contact length can be obtained by assuming that the point G at which plastic contact ends is located such that AG is parallel to the resultant force, F_R Fig. (3.3a).

Then, from geometry,

$$\frac{H}{\sin \theta} = \frac{1}{\sin(90 - (\alpha - \phi + \theta))} \quad (3.8)$$

from eqns. (3.6) and (3.8)

$$H = \frac{f \sin \theta}{\sin \theta \cdot \cos(\alpha - \phi + \theta)} \quad (3.9)$$

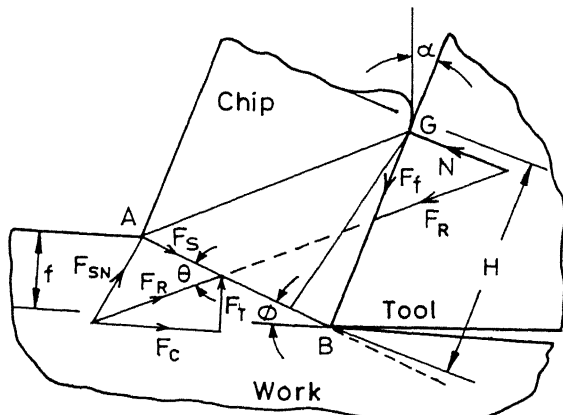


Fig. 3.3(a) Force diagram

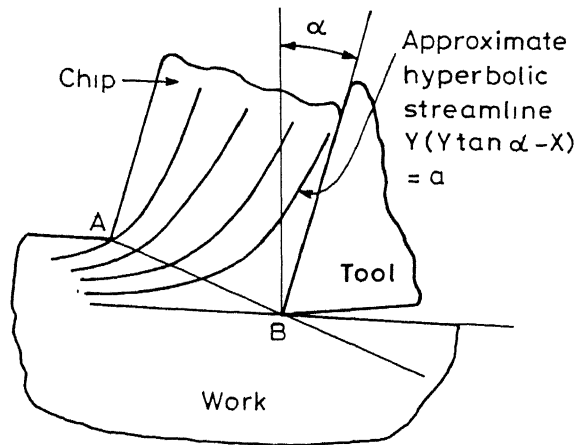


Fig. 3.3(b) Hyperbolic model of a streamline.

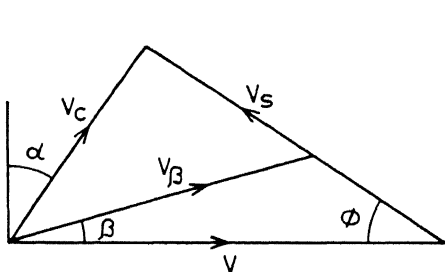


Fig. 3.4 Velocity diagram

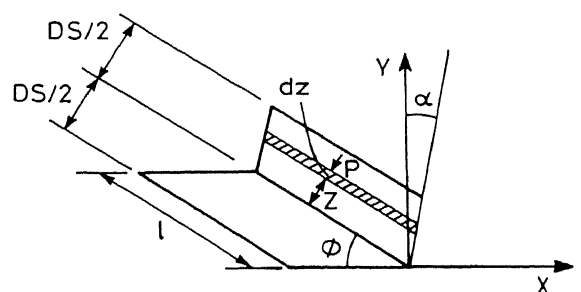


Fig. 3.5

3.3 VELOCITY FIELD:

3.3.(a) For Uncut Metal and Chip:

The velocity of uncut metal is the cutting speed (V) itself. So the velocity components for the uncut metal are:

$$u = V \quad (3)$$

$$v = 0 \quad (3)$$

where,

u = component of velocity along x-direction

v = component of velocity along y-direction.

The velocity components of fully formed chip are:

$$u = V_c \cdot \sin \alpha \quad (3.1)$$

$$v = V_c \cdot \cos \alpha \quad (3.1)$$

where,

$$V_c = V \cdot r .$$

V_c is chip velocity and r is chip thickness ratio.

3.3(b) Primary Shear Deformation Zone (PSDZ):

The hyperbolic streamline Fig.(3.3b) concept developed by Tay et al [8] is used for calculating the primary zone velocity. Strain-rate and heat generation-rate. According to this model, a material particle is considered to flow along a hyperbolic streamline curve in the PSDZ. The model is based on the following assumptions:

- (i) The direction of the maximum shear strain-rate is parallel to the shear plane.
- (ii) The overall change in velocity through PSDZ can be represented with sufficient accuracy by the velocity diagram Fig.(3.4).
- (iii) The distribution of maximum shear-strain rate along the normal to AB Fig. (3.3a) is symmetrical about AB with the maximum value occurring at AB.
- (iv) The strain-rate does not vary in a direction parallel to AB. Therefore, all streamlines passing through PSDZ can be taken to be similar in shape.

All the above said assumptions had been claimed to be verified experimentally by the authors of the model. Envolving these approximations, they have derived the equation (3.14) of the hyperbolic streamline

$$y(y \tan\alpha - x) = a \quad (3.14)$$

where,

$$a = \text{constant.}$$

Using velocity diagram, Fig. (3.4), velocity V_β at a point on a streamline is given by

$$V_\beta = \frac{V \sin \phi}{\sin(\phi + \beta)} \quad (3.15)$$

where β is the angle made by the streamline with the cutting direction. It is obtained by differentiating eq. (3.14) in the form,

$$\tan \beta = \frac{dy}{dx} = \frac{y}{2y \tan \alpha - x} \quad (3.16)$$

Velocity components are

$$u = V_\beta \cdot \cos \beta \quad (3.17)$$

$$v = V_\beta \cdot \sin \beta \quad (3.18)$$

The component of velocity parallel to AB, will be

$$V_{\beta \phi} = V_\beta \cdot \cos(\phi + \beta) \quad (3.19)$$

The strain rate is then calculated as:

$$\dot{\nu}_\beta = \frac{d V_{\beta \phi}}{dz} \quad (3.20)$$

where z is the distance of the concerned point from the mean plane AB, Fig.(3.5), and it can be seen that

$$z = x \sin \phi + y \cos \phi \quad (3.21)$$

From eqns. (3.14 - 3.21), we get,

$$\dot{\nu}_\beta = \frac{2a V \sin \phi}{[z^2 + 4a \sin^2 \phi (\tan \alpha + \cot \phi)]^{3/2}} \quad (3.22)$$

The constant 'a' of the eqn. (3.14) can be eliminated as follows.

The shear velocity reaches the value V_s within the chip from zero within the uncut metal. Thus, average work done per unit time in shearing the metal can be approximated as

$$w_s \approx \frac{F_s V_s}{2} \quad (3.23)$$

The work done per unit volume, w_s , can now be written as:

$$w_s = \frac{F_s}{dL(DS)} \cdot \frac{V_s}{2}$$

$$\approx \tau \cdot \frac{V_s}{2(DS)} \quad (3.24)$$

Based on the assumption of a constant yield shear stress in the PSDZ, the average shear strain rate can be shown to be

$$\dot{\gamma}_{av} \tau = w_s = \tau \cdot \frac{V_s}{2(DS)}$$

or

$$\dot{\gamma}_{av} = \frac{V_s}{2(DS)} \quad (3.25)$$

Referring Fig. (3.5) and eqn.(3.22), the average strain rate is also given by the expression:

$$\dot{\gamma}_{av} = \frac{2}{DS} \cdot \int_0^{\frac{DS}{2}} \dot{\gamma}_\beta dz$$

$$= \frac{2}{DS} \int_0^{\frac{DS}{2}} \frac{J}{(z^2 + K^2)^{3/2}} dz \quad (3.26)$$

where,

$$J = 2a V \sin\theta \quad (3.27)$$

and,

$$K^2 = 4a \sin^2\theta (\tan\alpha + \cot\theta) \quad (3.28)$$

Now,

$$\begin{aligned}\frac{J}{K^2} &= \frac{V \cos \alpha}{2 \cos(\theta - \alpha)} \\ &= \frac{V_s}{2} \quad (\text{using velocity diagram 3.4}) \quad (3.29)\end{aligned}$$

Integrating eqn.(3.26) with the substitution
 $z = K \tan \theta$, we get

$$\begin{aligned}\dot{\nu}_{av} &= \frac{2}{DS} \int_{z=0}^{\frac{DS}{2}} \frac{J}{K^2} \cdot \cos \theta \, d\theta \\ &= \frac{2}{DS} \cdot \frac{J \left(\frac{DS}{2} \right)}{K^2 \sqrt{\left(\frac{DS}{2} \right)^2 + K^2}}\end{aligned}$$

which, using eqn.(3.29) becomes

$$\dot{\nu}_{av} = \frac{V_s}{2 \sqrt{\left(\frac{DS}{2} \right)^2 + K^2}} \quad (3.30)$$

Equating eqns.(3.25) and (3.30),

$$K^2 = \frac{3}{4} (DS)^2. \quad (3.31)$$

So, strain rate can be written as

$$\dot{\nu}_{\beta} = \frac{J}{(z^2 + K^2)^{3/2}} \quad (3.32)$$

where,

J , K^2 and z are given by the eqns. (3.27), (3.28) and (3.21) respectively.

3.3(c) In Secondary Plastic Zone:

By analysing the deformation along the tool-chip interface obtained using printed grids with quick stop device (QSD), Tay et al [8] found that the sliding velocity of the chip at the interface could be given by the equation

$$V_{int} = \frac{1}{3} V_c \cdot \sqrt{1 + \frac{8S}{H}} \quad (3.33)$$

where,

S is the distance of the point concerned with the cutting edge measured along the interface Fig. (1.1).

Velocity in the secondary zone is linearly interpolated from V_{int} at interface to V_c at the fully developed chip.

The velocity field thus obtained is used in turn for calculating the strain rate and the heat generation rate within the secondary zone.

3.4 CALCULATION OF HEAT GENERATION:

In the primary zone, heat generation occurs due to plastic work only. In the secondary zone it occurs both due to plastic work and interfacial friction.

Assuming the shear stress to be uniform, the rate of heat generation per unit volume in the primary zone is calculated as

$$\dot{Q}_{PZ} = \frac{F_s}{1d} \cdot \dot{\nu}_\beta \quad (3.34)$$

The heat generation rate per unit volume in secondary zone [8] due to plastic work can be assumed to vary linearly from \dot{Q}_{SZintp} at interface to zero within the fully formed chip. The interfacial value \dot{Q}_{SZintp} is given by

$$\dot{Q}_{SZintp} = \frac{10 F_f V}{3 \delta t_2 (3H - b)d} \quad (3.35)$$

where,

$$b = \delta t_2 \cdot \tan(\theta - \alpha) \quad (3.36)$$

In secondary zone, frictional heat generation rate per unit volume is obtained by distributing total frictional energy over a small strip of average width, Δy , and length, H , in the form:

$$\Delta \dot{Q}_{SZF} = \frac{F_f \cdot V_c}{3Hd \Delta y} \sqrt{1 + \frac{8S}{H}} \quad (3.37)$$

CHAPTER 4

FINITE ELEMENT ANALYSIS

INTRODUCTION [18] :

Finite element method (FEM) is a powerful numerical technique for solving many problems of engineering importance, such as the heat conduction in solids, stress analysis for design etc. The FEM can be applied without much difficulty to problems with irregular geometries, complex boundary conditions and non-linear processes. The advantage of the FE procedure over other numerical techniques such as the finite difference method (FDM), is that general purpose computer programmes for an application may be developed through FEM, which can be applied to a wide variety of boundary conditions and geometries by just changing the input data. Due to these reasons, the FE solution technique was employed in the present work for predicting the temperature field during accelerated machining.

4.1 DESCRIPTION OF FE TECHNIQUE:

The solution steps in FE can be summarized as [18]:

- (a) obtain the equivalent integral equations from governing differential equations. The boundary conditions would be transformed into appropriate boundary, integrals,

(b) Divide the solution domain into subdivisions or elements. (Figure (4.1) shows such subdivisions to the problem analyzed in the present work). Place chosen number of nodes within each element and obtain approximating functions for describing the field variable, within each element, in terms of nodal values.

(c) Find the elemental matrices for the nodal values within each element.

(d) The elemental matrices are then assembled for all the elements, giving rise to global matrix equations for all the nodal values in the entire solution domain. These global matrix equations are solved to get the value of field variable at all the nodes.

Variational or Galerkin's procedure can be followed for converting the governing partial differential equations into equivalent integral equations.

The Galerkin's approach is used in the present work. Consider the differential equation of the form,

$$L(\phi) = 0 \quad (4.1)$$

where ϕ is the exact solution to the differential equation. However, approximation solution, ϕ^* , will leave behind a residue.

That is,

$$L(\emptyset^*) = R \quad (4.2)$$

where R is the residue which may be a function of the spatial co-ordinates. In Galerkin's procedure, the residue, weighted approximately by suitable weighting functions, is minimised over the whole solution domain D in an integral sense. In mathematical form, this becomes

$$\int_D W_i R \, dV = \int_D W_i L(\emptyset^*) \, dV = 0, \text{ for all } i \quad (4.3)$$

where W_i are the weighting functions. The approximation solution \emptyset^* may be written as a piecewise continuous profile for each element as:

$$\emptyset^*(e) = \sum_{i=1}^m N_i^{(e)} \emptyset_i^{(e)} \quad (4.4)$$

where m is the number of nodes per element. In the above equation, $N_i^{(e)}$ are the approximating functions for representing \emptyset^* within the element (e) and these are called the "shape functions" of the element (e) . The nodal values of \emptyset^* for the element (e) are denoted by $\emptyset_i^{(e)}$. In Galerkin's procedure, the weighting functions, W_i are taken to be the same as the shape functions $N_i^{(e)}$ within each element.

The governing differential equation for heat transfer during machining can be written in the form,

$$k \left(\frac{\partial^2 \bar{T}}{\partial x^2} + \frac{\partial^2 \bar{T}}{\partial y^2} \right) - \rho c_p (u \frac{\partial \bar{T}}{\partial x} + v \frac{\partial \bar{T}}{\partial y}) + \dot{Q} = \rho c_p \frac{\partial \bar{T}}{\partial t} \quad (4.4a)$$

Using an approximate temperature \bar{T} in eqn.(4.4a), we have,

$$L(\bar{T}) = k \left(\frac{\partial^2 \bar{T}}{\partial x^2} + \frac{\partial^2 \bar{T}}{\partial y^2} \right) - \rho c_p (u \frac{\partial \bar{T}}{\partial x} + v \frac{\partial \bar{T}}{\partial y}) + \dot{Q} - \rho c_p \frac{\partial \bar{T}}{\partial t} = R \quad (4.5)$$

For the Galerkin's formulation,

$$\sum_{e=1}^E \int \int N_i^{(e)} \left[k \left(\frac{\partial^2 \bar{T}}{\partial x^2} + \frac{\partial^2 \bar{T}}{\partial y^2} \right) - \rho c_p (u \frac{\partial \bar{T}}{\partial x} + v \frac{\partial \bar{T}}{\partial y}) + \dot{Q} - \rho c_p \frac{\partial \bar{T}}{\partial t} \right] dx dy = 0 \quad (4.6)$$

$i = 1, m$, where m is the number of nodes per element
and E is the total number of internal elements within the domain
D. Now,

$$\bar{T} = \sum_{j=1}^m N_j^{(e)} T_j^{(e)} \text{ for element (e)} \\ = [N^{(e)}] \{T_n^{(e)}\} \quad (4.7a)$$

where $[N^{(e)}]$ and $\{T_n^{(e)}\}$ are the vectors containing the shape
functions and nodal temperature values for element (e). For

representing \bar{T} over the whole solution domain. The above equation may be written as,

$$\bar{T} = \lfloor N \rfloor \{ T_n \} \quad (4.7b)$$

where $\lfloor N \rfloor$ is the overall shape function vector containing the piecewise continuous approximating functions and $\{ T_n \}$ is the total nodal temperature vector. Using eqn. (4.7a) in eqn. (4.6), we get

$$\begin{aligned} \sum_{e=1}^E \sum_{i=1}^m \int \int (e) [& k N_i^{(e)} \left(\frac{\partial^2 N_j^{(e)}}{\partial x^2} + \frac{\partial^2 N_j^{(e)}}{\partial y^2} \right) T_j^{(e)} \\ & - N_i^{(e)} \rho c_p (u \frac{\partial N_j^{(e)}}{\partial x} + v \frac{\partial N_j^{(e)}}{\partial y}) T_j^{(e)} \\ & + N_i^{(e)} \dot{Q} - N_i^{(e)} \rho c_p (N_j^{(e)} \frac{\partial T_j^{(e)}}{\partial t} \\ & + T_j^{(e)} \frac{\partial N_j^{(e)}}{\partial t})] dx dy = 0 \end{aligned} \quad (4.8a)$$

$$j = 1, m .$$

The integral in the above form would require the continuity of shape functions and its derivatives at all the interface regions, since second order derivatives of N_j occur in the equation (4.8a). It is useful to convert the above equation by making use of Green's theorem, so that lower order shape functions can be used for approximating the

temperature. The Green's theorem states that for two scalar functions f_1 and f_2 ,

$$\iiint_V \nabla \cdot (f_1 \nabla f_2) dV = \oint_S \mathbf{n} \cdot f_1 \nabla f_2 ds \quad (4.9)$$

or

$$\begin{aligned} \iiint_V [\nabla f_1 \cdot \nabla f_2 + f_1 \cdot \nabla^2 f_2] dV \\ = \oint_S f_1 \frac{\partial f_2}{\partial x_n} ds \end{aligned} \quad (4.9a)$$

using the above theorem for the functions N_i and \bar{T} ,

$$\begin{aligned} \iint_D k N_i \cdot \nabla^2 \bar{T} dV \\ = \oint_S k N_i \frac{\partial \bar{T}}{\partial x_n} ds \\ - \iiint_V k \left[\frac{\partial N_i}{\partial x} \cdot \frac{\partial \bar{T}}{\partial x} + \frac{\partial N_i}{\partial y} \cdot \frac{\partial \bar{T}}{\partial y} \right. \\ \left. + \frac{\partial N_i}{\partial z} \cdot \frac{\partial \bar{T}}{\partial z} \right] dx dy dz \end{aligned} \quad (4.10)$$

Combining the results of eqns.(4.10) and (4.8a) in 2-D co-ordinates, we get

$$\begin{aligned} - \iint_D k \left[\frac{\partial N_i}{\partial x} \cdot \frac{\partial T_n}{\partial x} + \frac{\partial N_i}{\partial y} \cdot \frac{\partial T_n}{\partial y} \right] \{T_n\} dx dy \\ + \rho k N_i \frac{\partial T_n}{\partial x_n} \{T_n\} dl + \iint_D \dot{Q} N_i dx dy \\ - \iint_D \rho c_p N_i [u \frac{\partial T_n}{\partial x} + v \frac{\partial T_n}{\partial y}] \{T_n\} dx dy \end{aligned}$$

$$\begin{aligned}
 & - \iint_D \rho c_p N_i \left[[N] \left\{ \frac{\partial T_n}{\partial t} \right\} + \frac{\partial [N]}{\partial t} \left\{ T_n \right\} \right] dx dy \\
 & = 0 \tag{4.11}
 \end{aligned}$$

On the boundary (boundary conditions used for present work is shown in Fig. (4.2) of the solution domain D, we get

$$\begin{aligned}
 & \int k N_i \frac{\partial T}{\partial x_n} dl \\
 & = - \int_{S_q} N_i \left[-k \frac{\partial T}{\partial x_n} \right] dl \\
 & - \int_{S_h} \left[N_i -k \frac{\partial T}{\partial x_n} \right] dl \\
 & = - \int_{S_q} N_i q dl - \int_{S_h} N_i h (T - T_o) dl \\
 & = - \int_{S_q} N_i q dl + \int_{S_h} N_i h T_o dl \\
 & - \int_{S_h} N_i h T dl \\
 & = - \int_{S_q} N_i q dl + \int_{S_h} N_i h T_o dl \\
 & - \int_{S_h} N_i h [N] \{ T_n \} dl \tag{4.12}
 \end{aligned}$$

Therefore,

$$\begin{aligned}
 \iint_D R N_i dA & = - \iint_D \left[k \left(\frac{\partial N_i}{\partial x} \cdot \frac{\partial [N]}{\partial x} + \frac{\partial N_i}{\partial y} \frac{\partial [N]}{\partial y} \right) \right. \\
 & \left. + \rho c_p N_i (u \frac{\partial [N]}{\partial x} + v \frac{\partial [N]}{\partial y} + \frac{\partial [N]}{\partial t}) \right]
 \end{aligned}$$

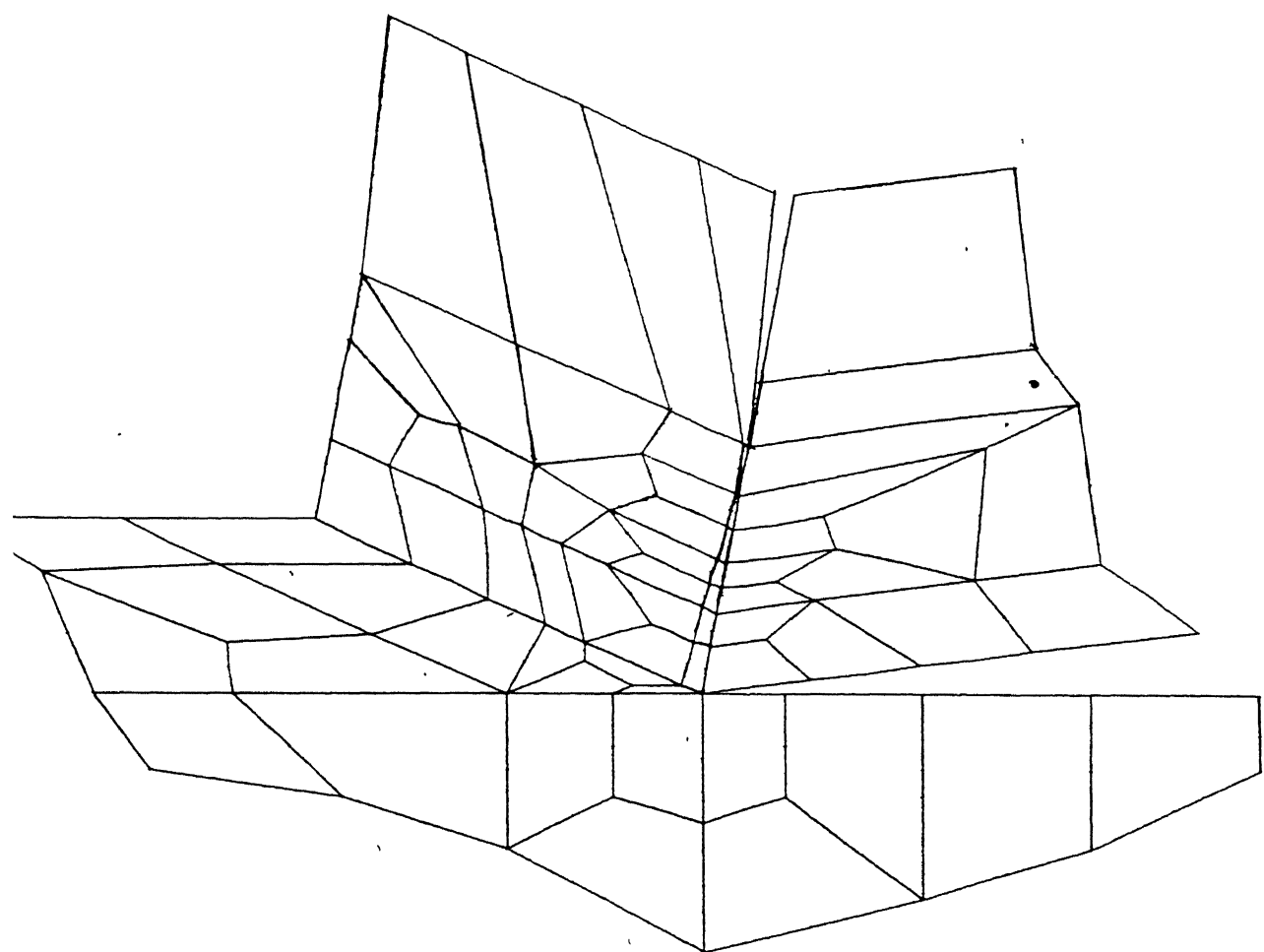


FIG. 4.1 FINITE ELEMENT MESH

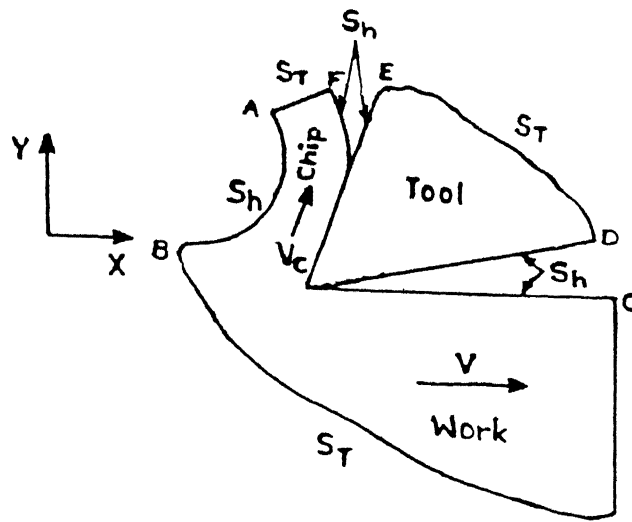
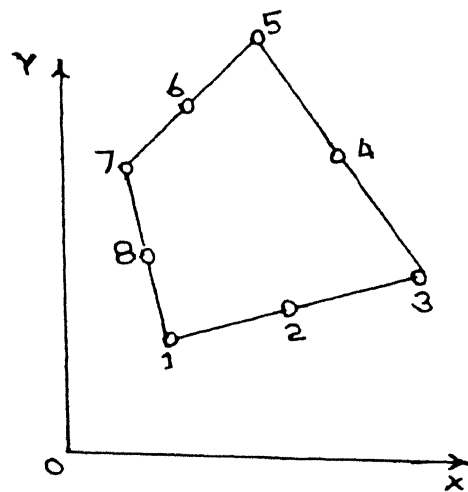
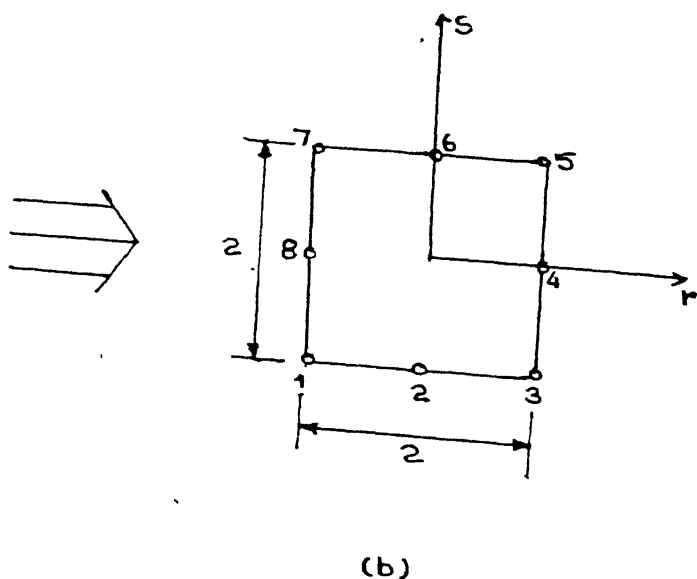


Fig. 4.2 Problem region, showing the thermal boundary conditions.



(a)



(b)

Fig 4.3 Finite Element in
 (a) x-y domain
 (b) r-s domain

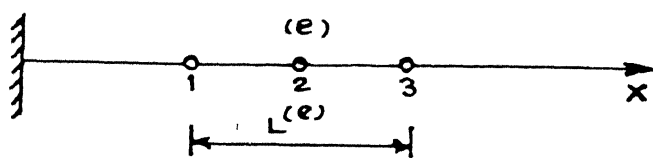


Fig. 4.4 A typical boundary (line) element

$$\begin{aligned}
 & \int dx \int dy \{T_n\} + \iint_D \rho c_p N_i [N] dx dy \{ \frac{\partial T_n}{\partial t} \} \\
 & - \int_{S_h} h N_i [N] \{T_n\} dl - \int_{S_q} N_i q dl \\
 & + \int_{S_h} N_i h T_o dl + \iint_D \dot{Q} N_i dx dy = 0
 \end{aligned} \quad (4.13)$$

The eqn.(4.13) can be written down in the matrix form as,

$$[H] \{T_n\} + [M] \{ \frac{\partial T_n}{\partial t} \} = \{F\} \quad (4.14)$$

where, for the matrices $[H]$ and $[M]$, and vector $\{F\}$, the elements are given by

$$H_{ij}^{(e)} = K_{ij}^{(e)} + H_{1ij}^{(e)} \quad (4.14a)$$

where,

$$H_{1ij}^{(e)} = (e) \int h N_i N_j dl \quad (4.15)$$

$$\begin{aligned}
 K_{ij}^{(e)} &= (e) \left[k \left(\frac{\partial N_i}{\partial x} \cdot \frac{\partial N_j}{\partial x} + \frac{\partial N_i}{\partial y} \cdot \frac{\partial N_j}{\partial y} \right) \right. \\
 &+ \rho c_p (u N_i \frac{\partial N_j}{\partial x} + v N_i \frac{\partial N_j}{\partial y} \\
 &\left. + \frac{\partial N_j}{\partial t}) \right] dx dy
 \end{aligned} \quad (4.15a)$$

This can be written as

$$[H] = \sum_{e=1}^E [H^{(e)}] \quad (4.15b)$$

$$= \sum_{e=1}^E [K^{(e)}] + \sum_{e=1}^{E_h} [H_1^{(e)}] \quad (4.15c)$$

$$M_{ij}^{(e)} = \iint_{(e)} \rho c_p N_i N_j dx dy \quad (4.16a)$$

This can be written as

$$[M] = \sum_{e=1}^E [M^{(e)}] \quad (4.16b)$$

$$\begin{aligned} F_i^{(e)} = & \iint_{(e)} \dot{Q} N_i dx dy - \left(\int_{(e)} N_i q dl \right. \\ & \left. + \int_{(e)} N_i h T_o dl \right) \end{aligned} \quad (4.17a)$$

which can be written as

$$\begin{aligned} \{F\} = & \sum_{e=1}^E \{\dot{Q}^{(e)}\} + \sum_{e=1}^{E_q} \{q_B^{(e)}\} \\ & + \sum_{e=1}^{E_h} \{H_2^{(e)}\} \end{aligned} \quad (4.17b)$$

where,

$$i = 1, 2, \dots, m$$

$$j = 1, 2, \dots, m$$

and E_q , E_h are respectively the number of boundary elements having applied heat flux and convective boundary conditions.

In eqn. (4.17b)

$$\{\dot{Q}^{(e)}\} = \iint_{(e)} \dot{Q} N_i dx dy \quad (4.18a)$$

$$\{q_B^{(e)}\} = \int_e N_i q \, dl \quad (4.18b)$$

$$\{H_2^{(e)}\} = \int_e N_i h T_0 \, dl \quad (4.18c)$$

4.2 SHAPE FUNCTIONS AND THEIR LOCAL DERIVATIVES:

In the present work, 8-noded quadrilateral isoparametric elements are used for spatial discretization of solution domain Fig. (4.3).

Let (x_i, y_i) be the cartesian co-ordinates of i^{th} node in $x-y$ domain and after mapping the element in $r-s$ domain (r_i, s_i) are its natural co-ordinates. Then natural and cartesian co-ordinates are related by

$$\begin{Bmatrix} x \\ y \end{Bmatrix} = \begin{bmatrix} N & 0 \\ 0 & N \end{bmatrix} \begin{Bmatrix} x_n \\ y_n \end{Bmatrix} \quad (4.18d)$$

where,

$$x_n = \begin{Bmatrix} x_1 \\ x_2 \\ \vdots \\ x_8 \end{Bmatrix} \quad (4.18e)$$

$$y_n = \begin{Bmatrix} y_1 \\ y_2 \\ \vdots \\ y_8 \end{Bmatrix} \quad (4.18f)$$

$$N = \begin{bmatrix} N_1 & N_2 & \dots & N_8 \end{bmatrix} \quad (4.18g)$$

N_i 's are functions of r, s and given by (4.21a - 4.21g)

$$0 = [0 \ 0 \ 0 \ \dots \ 0] \quad (4.18h)$$

Temperature within each element is in the form

$$\begin{aligned} T = & a_0 + a_1 x + a_2 y + a_3 x^2 + a_4 y^2 + a_5 xy \\ & + a_6 x^2 y + x_7 x y^2. \end{aligned} \quad (4.19)$$

In terms of the nodal values of temperature and the shape functions, we can write eqn. (4.19) as

$$T = \sum_{i=1}^8 N_i T_i \quad (4.20)$$

where,

$$N_1 = 0.25 (-1 + rs + r^2 - r^2s - rs^2) \quad (4.21a)$$

$$N_2 = 0.5 (1 - s - r^2 + r^2s) \quad (4.21b)$$

$$N_3 = 0.25 (-1 - rs + r^2 + s^2 - r^2s + rs^2) \quad (4.21c)$$

$$N_4 = 0.5 (1 + r - s^2 - rs^2) \quad (4.21d)$$

$$N_5 = 0.25 (-1 + rs + r^2 + s^2 + r^2s + rs^2) \quad (4.21e)$$

$$N_6 = 0.5 (1 + s - r^2 - r^2s) \quad (4.21f)$$

$$N_7 = 0.25 (-1 - rs + r^2 + r^2s - rs^2) \quad (4.21g)$$

$$N_8 = 0.5 (1 - r - s^2 + rs^2) \quad (4.21h)$$

Differentiating the expressions (4.21a - 4.21h) partially with respect to r and s , we get local derivatives of shape

functions as,

$$\frac{\partial N_1}{\partial r} = 0.25 (s + 2r - 2rs - s^2) \quad (4.22a)$$

$$\frac{\partial N_2}{\partial r} = -r + rs \quad (4.22b)$$

$$\frac{\partial N_3}{\partial r} = 0.25 (-s + 2r - 2rs + s^2) \quad (4.22c)$$

$$\frac{\partial N_4}{\partial r} = 0.5 (1 - rs) \quad (4.22d)$$

$$\frac{\partial N_5}{\partial r} = 0.25 (s + 2r + 2rs + s^2) \quad (4.22e)$$

$$\frac{\partial N_6}{\partial r} = -r - rs \quad (4.22f)$$

$$\frac{\partial N_7}{\partial r} = 0.25 (-s + 2r + 2rs - s^2) \quad (4.22g)$$

$$\frac{\partial N_8}{\partial r} = 0.5 (-1 + s^2) \quad (4.22h)$$

$$\frac{\partial N_1}{\partial s} = 0.25 (r + 2s - r^2 - 2rs) \quad (4.23a)$$

$$\frac{\partial N_2}{\partial s} = 0.5 (-1 + r^2) \quad (4.23b)$$

$$\frac{\partial N_3}{\partial s} = 0.25 (-r + 2s - r^2 + 2rs) \quad (4.23c)$$

$$\frac{\partial N_4}{\partial s} = -s - rs \quad (4.23d)$$

$$\frac{\partial N_5}{\partial s} = 0.25 (r + 2s + r^2 + 2rs) \quad (4.23e)$$

$$\frac{\partial N_6}{\partial s} = 0.5 (1 - r^2) \quad (4.23f)$$

$$\frac{\partial N_7}{\partial s} = 0.25 (-r + 2s + r^2 - 2rs) \quad (4.23g)$$

$$\frac{\partial N_8}{\partial s} = -s + rs \quad (4.23h)$$

4.3 GLOBAL DERIVATIVES AND NUMERICAL INTEGRATION:

(a) Global Derivatives: If G is a scalar function of the natural co-ordinates r and s , its derivatives with respect to x and y can be given by

$$\frac{\partial G}{\partial r} = \frac{\partial G}{\partial x} \cdot \frac{\partial x}{\partial r} + \frac{\partial G}{\partial y} \cdot \frac{\partial y}{\partial r} \quad (4.24a)$$

$$\frac{\partial G}{\partial s} = \frac{\partial G}{\partial x} \cdot \frac{\partial x}{\partial s} + \frac{\partial G}{\partial y} \cdot \frac{\partial y}{\partial s} \quad (4.24b)$$

from which

$$\begin{Bmatrix} \frac{\partial G}{\partial x} \\ \frac{\partial G}{\partial y} \end{Bmatrix} = [J]^{-1} \begin{Bmatrix} \frac{\partial G}{\partial r} \\ \frac{\partial G}{\partial s} \end{Bmatrix} \quad (4.25a)$$

where $[J]$ is a 2×2 matrix, called the Jacobian matrix, given by

$$[J] = \begin{bmatrix} \frac{\partial x}{\partial r} & \frac{\partial y}{\partial r} \\ \frac{\partial x}{\partial s} & \frac{\partial y}{\partial s} \end{bmatrix} \quad (4.25b)$$

Using eqns. (4.18d) -(4.18h))

$$[J] = \begin{bmatrix} \frac{\partial N_1}{\partial r} & \frac{\partial N_2}{\partial r} & \cdots & \frac{\partial N_8}{\partial r} \\ \frac{\partial N_1}{\partial s} & \frac{\partial N_2}{\partial s} & \cdots & \frac{\partial N_8}{\partial s} \end{bmatrix} \begin{Bmatrix} x_1 & y_1 \\ x_2 & y_2 \\ \vdots & \vdots \\ x_8 & y_8 \end{Bmatrix} \quad (4.25c)$$

Putting G as N in (4.25a), the global derivatives of shape

functions can be written as

$$\begin{bmatrix} \frac{\partial [N]}{\partial x} \\ \frac{\partial [N]}{\partial y} \end{bmatrix} = [J]^{-1} \begin{bmatrix} \frac{\partial [N]}{\partial r} \\ \frac{\partial [N]}{\partial s} \end{bmatrix} \quad (4.26)$$

(b) Numerical Integration: In order to get the elemental matrices, the area integrals in the eqns. (4.16a), (4.17a), (4.15) etc. have to be evaluated, which are in the form

$$(e) \iint f (N_i, \frac{\partial N_i}{\partial x}, \frac{\partial N_i}{\partial y}, \dots) dx dy. \quad (4.27)$$

The quadrilateral region in the physical co-ordinates (x, y) has been mapped into square region in the natural co-ordinates, and the global derivatives $\frac{\partial}{\partial x}, \frac{\partial}{\partial y}$ as a functions of natural co-ordinates are known, therefore, these integrals can be written in the form

$$I = \int_{-1}^1 \int_{-1}^1 g(r, s) dr ds \quad (4.28)$$

where,

$dr ds$ is given by

$$dx dy = \det. [J] dr ds \quad (4.28a)$$

Now integrals in the above form can be evaluated numerically by using Gauss quadrature formula, taking 9 Gauss points per element

$$I = \sum_{i=1}^n \sum_{j=1}^n w_i w_j f(r_i, s_j) \quad (4.29)$$

where,

the number of Gauss points in one direction,

$$n = 3$$

and $w_i \cdot w_j$ is the weight at Gauss point (r_i, s_j) .

For 3-Gauss point quadrature in one direction

$$s_1, s_3 = r_1, r_3 = \pm 0.77459 \quad (4.30)$$

$$s_2 = r_2 = 0.00000 \quad (4.31)$$

$$w_1 = w_3 = 0.55555 \quad (4.32)$$

$$w_2 = 0.88888 \quad (4.33)$$

4.4 EVALUATION OF BOUNDARY INTEGRALS:

Referring to the boundary element shown in Fig. (4.4),

The x co-ordinate of any point on the line element is given by

$$x = r_1 x_1 + r_3 x_3 \quad (4.34)$$

where,

$$r_1 = 1 - \frac{x}{L(e)} \quad (4.35)$$

$$r_2 = \frac{x}{L(e)} \quad (4.36)$$

A 98936

x_1, x_3 = the co-ordinates of extreme nodes
 $L^{(e)}$ = length of element.

Then,

$$\int_0^{L^{(e)}} x_1^m x_2^n dx = \frac{m! n!}{(m+n+1)!} \cdot L^{(e)} \quad (4.37)$$

Shape functions for the element are

$$N_1 = x_1(2x_1 - 1) \quad (4.38a)$$

$$N_2 = 4x_1 x_2 \quad (4.38b)$$

$$N_3 = x_2(2x_2 - 1) \quad (4.38c)$$

Using the results of eqns. (4.37 - 4.38c), the boundary integrals in the eqns. (4.15), (4.18b) and (4.18c) can be found as:

$$[H_1^{(e)}] = \frac{L^{(e)} h}{30} \begin{bmatrix} 4 & 2 & -1 \\ 2 & 16 & 2 \\ -1 & 2 & 4 \end{bmatrix} \quad (4.39)$$

$$\{H_2^{(e)}\} = \frac{L^{(e)} h T_0}{6} \begin{Bmatrix} 1 \\ 4 \\ 1 \end{Bmatrix} \quad (4.40)$$

$$\{q_B^{(e)}\} = \frac{L^{(e)} q}{6} \begin{Bmatrix} 1 \\ 4 \\ 1 \end{Bmatrix} \quad (4.41)$$

4.5 SOLUTION OF SIMULATIONS LINEAR DIFFERENTIAL EQUATIONS:

To solve eqn. (4.14) for nodal temperature finite difference method is used for time domain.

Taking part of forward and part of backward time derivative temperature at $(n+1)^{th}$ level and n^{th} level are related by

$$\{T_n\}^{n+1} - \theta \Delta t \left\{ \frac{\partial T_n}{\partial t} \right\}^{n+1} = \{T_n\}^n + (1-\theta) \Delta t \left\{ \frac{\partial T_n}{\partial t} \right\}^n \quad (4.42)$$

where,

Δt = time step

$\theta = 1$, for fully backward or implicit scheme

$= 0$, for fully forward or explicit scheme

$= \frac{1}{2}$, for semiimplicit scheme.

Multiplying eqn. (4.42) by M^{n+1} and using implicit scheme, it can be written as:

$$[M]^{n+1} \{T_n\}^{n+1} - \Delta t [M] \left\{ \frac{\partial T_n}{\partial t} \right\}^{n+1} = [M]^{n+1} \{T_n\}^n \quad (4.43)$$

From eqn. (4.14),

$$[M]^{n+1} \left\{ \frac{\partial T_n}{\partial t} \right\}^{n+1} = \{F\}^{n+1} - [H] \{T_n\}^{n+1} \quad (4.44)$$

From eqns. (4.43) and (4.44)

$$([M]^{n+1} + \Delta t [H]^{n+1}) \{T_n\}^{n+1} = [M]^{n+1} \{T_n\}^n + \Delta t \{F\}^{n+1} \quad (4.45)$$

Thus, knowing nodal temperatures at n^{th} level it can be updated at $n+1^{th}$ level. Using eqn. (4.45).

4.6 AVERAGE TEMPERATURE ALONG TOOL-CHIP INTERFACE:

Envoing the parabolic variations along a 3-noded line element (Fig.(4.4)), average temperature along tool-chip interface can be written as

$$T_{av.} = \frac{1}{H} \sum_{e=1}^{E_{int}} \int_{(e)}^{L^{(e)}} T \, dl \quad (4.46)$$

where,

H = chip contact at length

E_{int} = number of line elements along interface

$L^{(e)}$ = length of element (e) .

Using the results of eqn. (4.40), we can write eqn.(4.46) as

$$T_{av.} = \frac{1}{H} \sum_{e=1}^{E_{int}} \cdot \frac{L^{(e)}}{6} \left\{ \begin{array}{c} T_1 \\ 4T_2 \\ T_3 \end{array} \right\}^{(e)} \quad (4.47)$$

where T_1 , T_2 , T_3 are the temperatures at local nodes 1, 2 and 3 respectively for the element (e).

CHAPTER V

RESULTS AND DISCUSSION

A general purpose finite element programme has been developed to determine the temperature distribution in tool-chip-work system and average tool-chip interface temperature under steady state condition (i.e., longitudinal turning) as well as transient situation (i.e., accelerated cutting) for a wide range of cutting conditions. The results obtained have been compared with experimental [12] and analytical [9] results to test the validity of present model. The experimental cutting data are borrowed from the work of other researchers (the details are given in Appendix I). The variation in temperature within the tool chip-workpiece system is illustrated by drawing isotherms. In order to investigate the effects of shear strain acceleration and its governing parameters on mean tool-chip interface temperature and temperature distribution in tool-chip-work system, accelerated test results have been compared with that of longitudinal turning.

5.1.1 COMPARISON OF PRESENT MODEL WITH OTHER ANALYTICAL MODEL:

Table 5.1 shows the comparison of the maximum temperature obtained using present analytical model and the results obtained by Murarka et al. [9]. It is clear from

TABLE 5.1 : Comparison of Maximum Temperature Obtained, Using Present Model and Other Analytical Model during Longitudinal Turning

S.No.	Test identi- fica- tion	N (r.p.m.)	V (m/min)	f (mm /rev.)	α (deg)	Tool- material (mm)	d (mm)	ϕ (deg)	F_c (N)	F_t (N)	Maximum temper- ature obtained ($^{\circ}\text{C}$)	
											Present work	Murarka [9] work
1	6	80	24.73	0.3556	20	HSS	6.35	39.0	3525	1560	585	527
2	1	80	24.73	0.3556	41	HSS	6.35	48.5	2425	280	525	470
3	13	80	24.73	0.3556	30	HSS	6.35	35.0	2650	545	450	413
4	5	57	17.34	0.3556	41	HSS	6.35	37.0	2300	256	431	396

TABLE 5.1.1 Comparison of $T_{\text{av.}}$ obtained using present work with that obtained by Balaji [11]

α (degree)	N (r.p.m)	Dia. (mm)	V (m/min)	Tool material	Work material	f (mm/rev.)	$T_{\text{av.}}$		Present work
							Experimental	Theoretical	
10	500	98	154	WC	MS	0.325	590 $^{\circ}\text{C}$	580 $^{\circ}\text{C}$	549 $^{\circ}\text{C}$

the table that the difference in temperature obtained by these two model ranges from 35°C to 58°C (about 8-10%), but the trend seems to be the same. Further temperature obtained using present work are always less than those obtained by Murarka [9]. This discrepancy could be attributed to the difference in the formulation of the problem. Murarka determined the velocity and strain rates experimentally using grid technique. The calculated tool-chip plastic contact length using experimental data. The present model does not require any of these experimental data. They have been calculated as described in Chapter 3. The value of maximum temperature is also governed by the fineness of the mesh in the critical zone (around the maximum temperature). The result is also compared with that obtained by Balaji [11] as shown in the table 5.1, page 56. The result is in good comparison.

5.1.2 COMPARISON WITH EXPERIMENTAL RESULTS:

The variation of the average tool-chip interface temperature (both analytical and experimental [12]) with cutting speed for longitudinal turning and facing test are shown in Figs. (5.1a) and (5.1b) respectively. In longitudinal turning, the experimental and theoretical results are quite close to each other. The difference in temperature values ranges approximately from 5 to 15%. In facing, the temperature obtained theoretically is lower than the experimental values by an amount equal to about 15 to 25%. From these figures, it is clear that both the curves, experimental and theoretical,

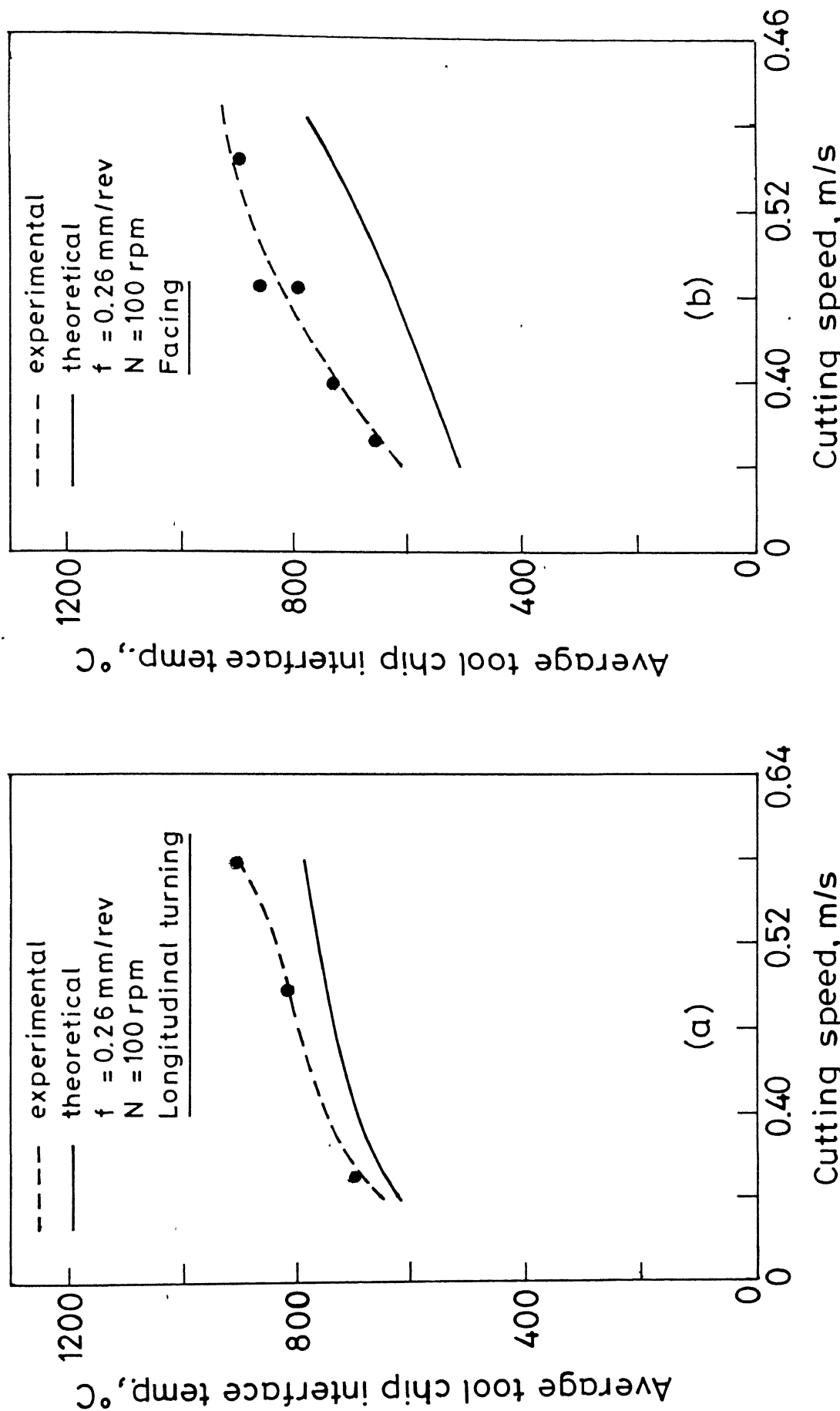


Fig. 5.1 Comparison of analytical and experimental average temperature.

of temperature. Also, formations of BUE and oxide layers at the interface may yield misleading results. Thus, the use of thermocouple method for measuring the tool-chip interface temperature is not fully reliable.

5.2 TEMPERATURE DISTRIBUTION:

The variation in temperature within the tool, chip and workpiece obtained using FE model is shown by isotherms for taper turning, facing and longitudinal turning in Figs. 5.2a, 5.2b and 5.3 respectively. These results were obtained for cutting conditions shown in the figures.

The isotherms in Figs. (5.2, 5.3) show that high temperature regions are the regions in the vicinity of the tool-chip interface. The lower temperature isotherms are located in the regions away from the interface. It may be explained as follows. High temperature regions are located near tool-chip interface because of the fact that the sum of frictional heat generated at tool-chip interface and heat generated due to chip deformation in secondary deformation zone is much higher than that of heat generated due to plastic deformation in PSDZ. The other reason for low temperature isotherms in and around PSDZ is that the large amount of heat generated in PSDZ due to plastic deformation is carried away by chip, and remaining is conducted in tool and work.

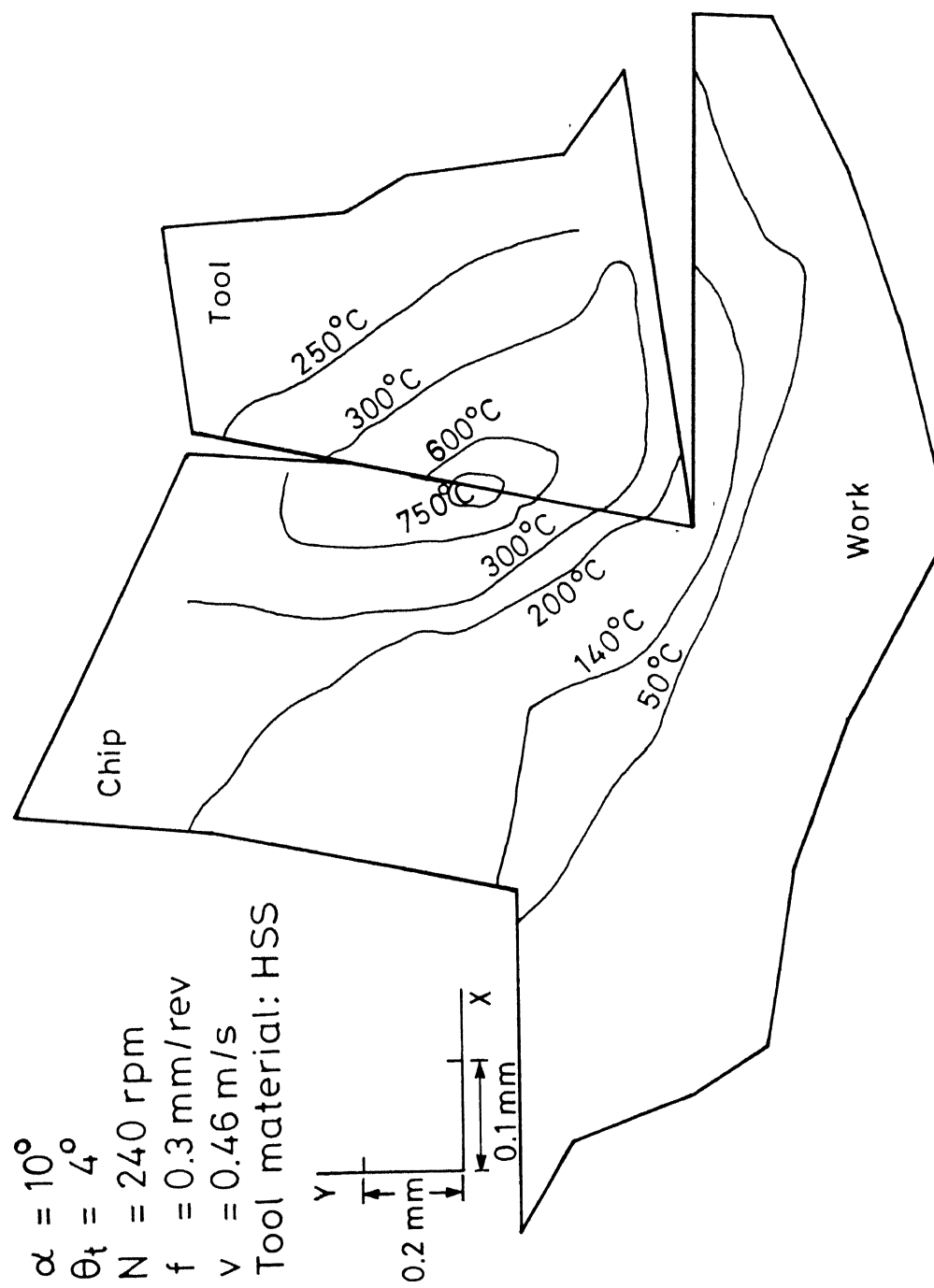


Fig. 5.2 (a) Temperature distribution in taper turning.

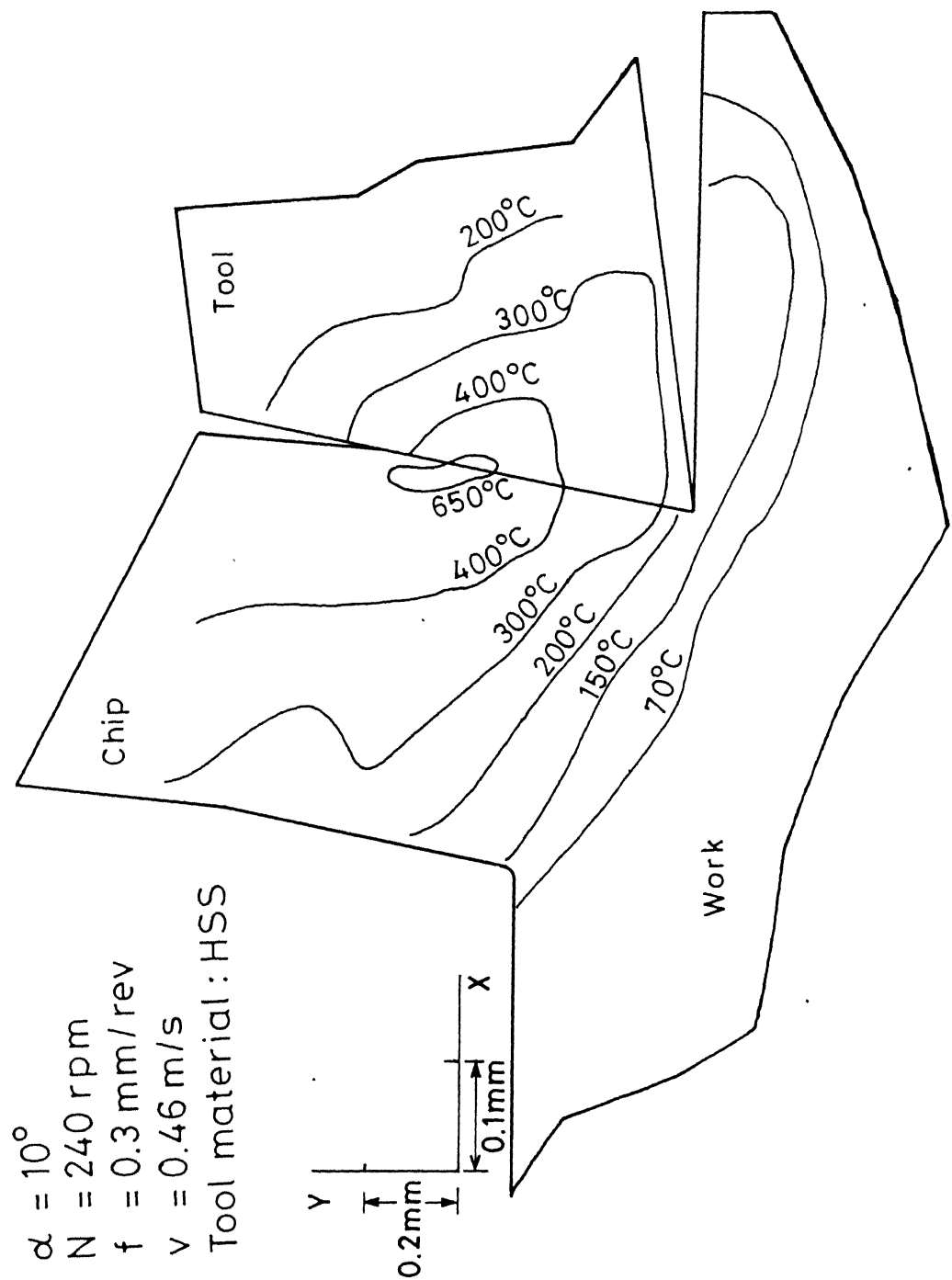


Fig. 5.2 (b) Temperature distribution in facing.

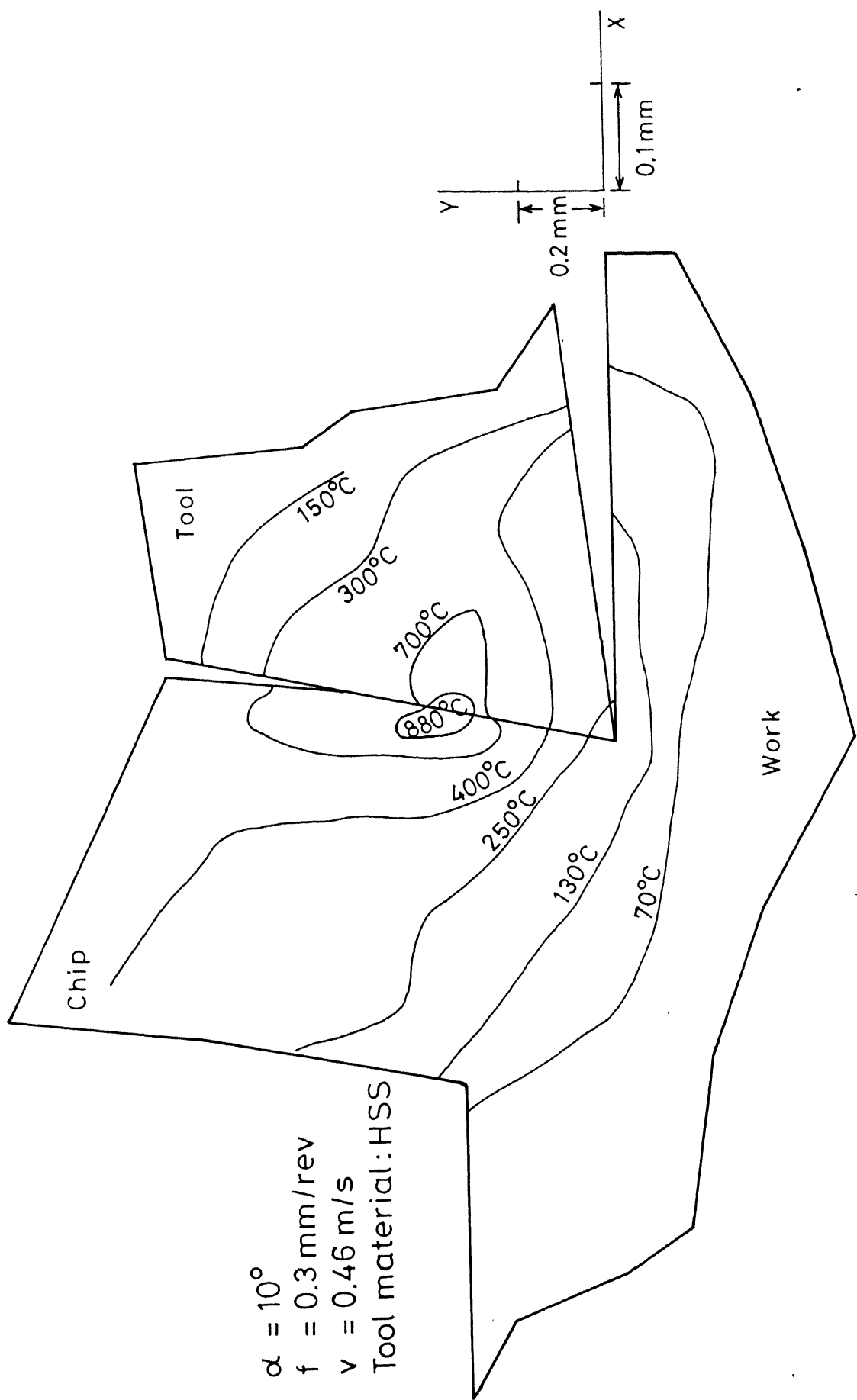


Fig. 5.3 Temperature distribution in longitudinal turning.

Figures 5.4(a) and 5.4(b) show the variation of temperature during longitudinal turning, taper turning and facing along rake and flank face. It is evident from the figures that in the beginning, the temperature profile increases steeply with the increase in distance from the cutting edge along rate face. It attains a maximum value at a distance of about 0.6-0.7 times the tool-chip contact length, thereafter it starts decreasing. The steep increase near the cutting edge is due to high heat generation rate in the secondary zone. But, beyond the maximum temperature point, the heat generation rate is smaller as compared to rate of heat loss due to conduction. Therefore, the temperature decreases with the increase in distance away from the maxima. The secondary deformation zone ends at a point where the tool and chip contact ends. Beyond this point, there is no heat generation, but there is heat loss due to conduction, and convection to the atmosphere. Therefore, the temperature goes on decreasing with the increase in distance.

Almost similar pattern of variation in temperature along flank face is also observed. However, the magnitude of highest temperature and slope of temperature profile slightly differ in the two cases. The increase in temperature may be attributed to the fact that heat generation in the secondary zone also affects flank face temperature near the cutting edge. Also, there is some amount of heat generation due to friction between flank face and machined surface, however this has not been taken into account in the present model.

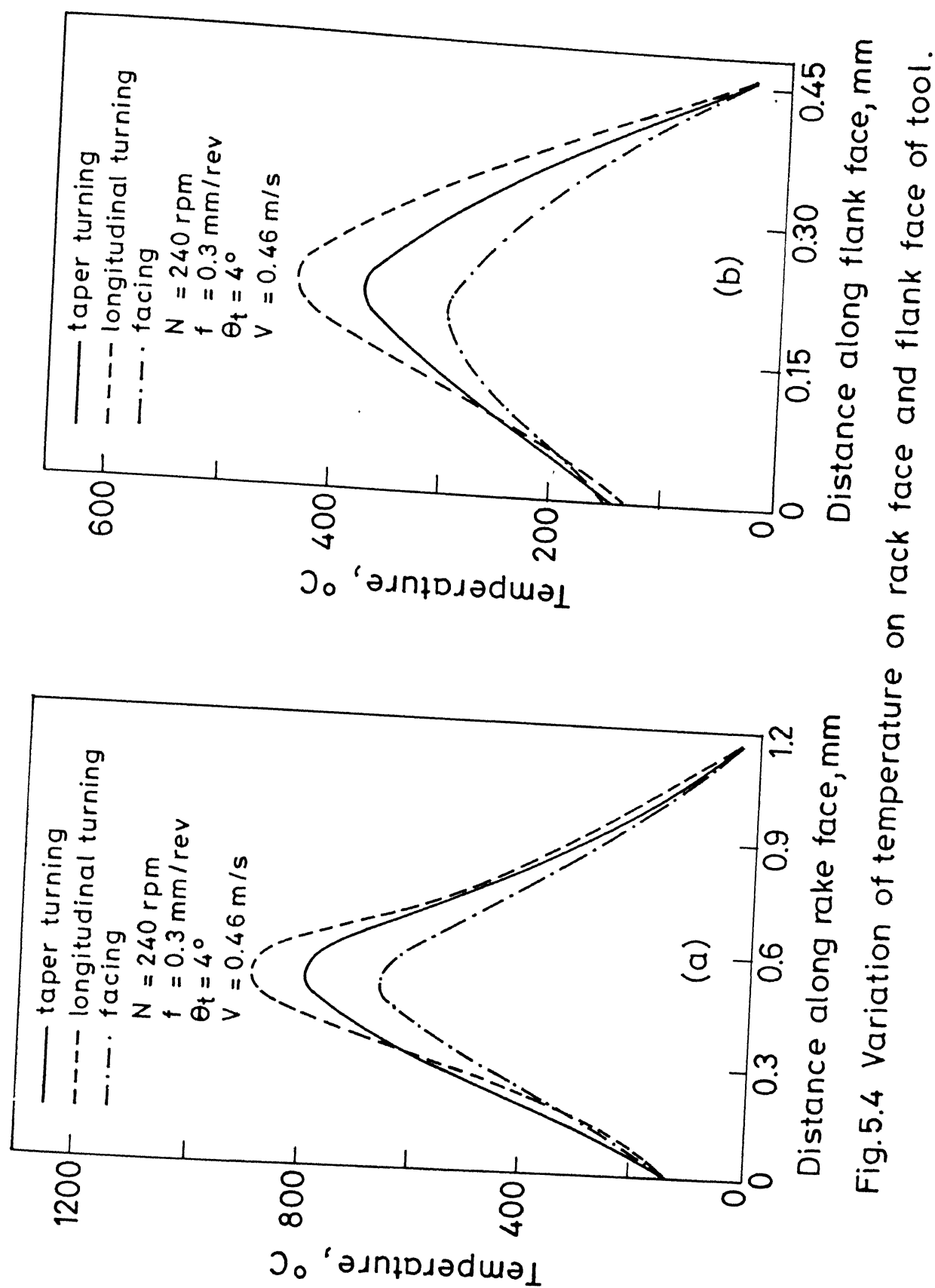


Fig. 5.4 Variation of temperature on rack face and flank face of tool.

Then a fall of temperature is expected as one moves away from the cutting edge as a result of the heat loss due to conduction and convection.

The similar trends (Fig. 5.4) of variation in temperature along rake and flank face have been reported by others [9, 11]. In both the figures 5.4(a) and 5.4(b), it is also observed that the temperature attained at a distance from the cutting edge is highest in case of longitudinal turning lowest in case of facing and in between the two (longitudinal and facing) in case of taper turning. This conclusion is in line with the experimental observations reported in reference [12] and [20] about the average tool-chip interface temperature. $T_{av.}$ has been calculated using 68 elements and 22 elements mesh. The difference in the result in two cases were ~~as~~ very small.

5.3 PARAMETRIC STUDY IN LONGITUDINAL TURNING AND ACCELERATED CUTTING:

To study the effects of strain acceleration governing parameters on mean tool-chip interface temperature during longitudinal turning and accelerated cutting, parametric studies has been made.

Variation of average tool-chip interface temperature with feed rate and cutting speed, for longitudinal turning as well as accelerated cutting (viz. taper-turning and facing) are shown in Figs. 5.5a and 5.5b respectively. It is clear from the figures that the average temperature in all the

Three cases, increases with the increase in feed rate and cutting speed. However, the magnitude of temperature is seen to be the highest in case of longitudinal turning and lowest in case of facing at any machining condition. The similar trends have been observed by the investigators [12] and [20] as shown in Figs. 5.6a and 5.6b respectively.*

Figure 5.5c shows the variation in average tool-chip interface temperature with taper angle in case of taper turning. The longitudinal turning and facing temperature results for the same cutting conditions (except the taper angle) are also shown in the Fig. 5.5c. It is clear from the figure that the temperature decreases with the increase in taper angle.

The variation of average tool-chip interface temperature with spindle speed is shown in Fig. 5.5d. It is observed that the temperature increases with an increase in spindle speed in case of accelerated cutting.

* The nature of variation of temperature rise in the tool chip interface is very well known to be parabolic with cutting speed (in the form $T_{av.} \propto \sqrt{V}$) for longitudinal turning (Ref. [4]), whereas the trend observed here is not similar. The possible reason for discrepancy could be the forces input taken from ref. [17].

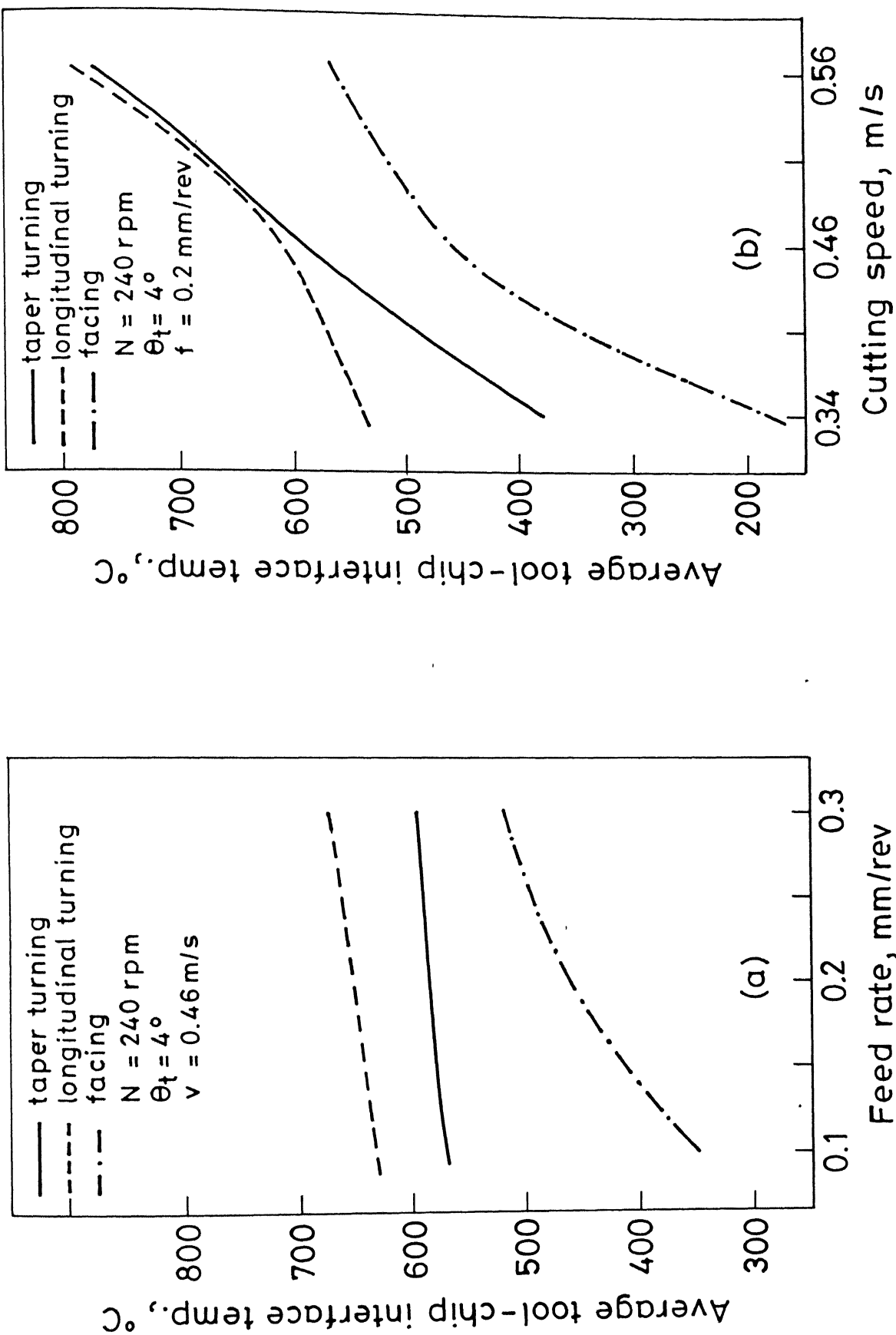


Fig. 5.5 Comparison of tool-chip interface temperature during longitudinal turning, taper turning and facing.

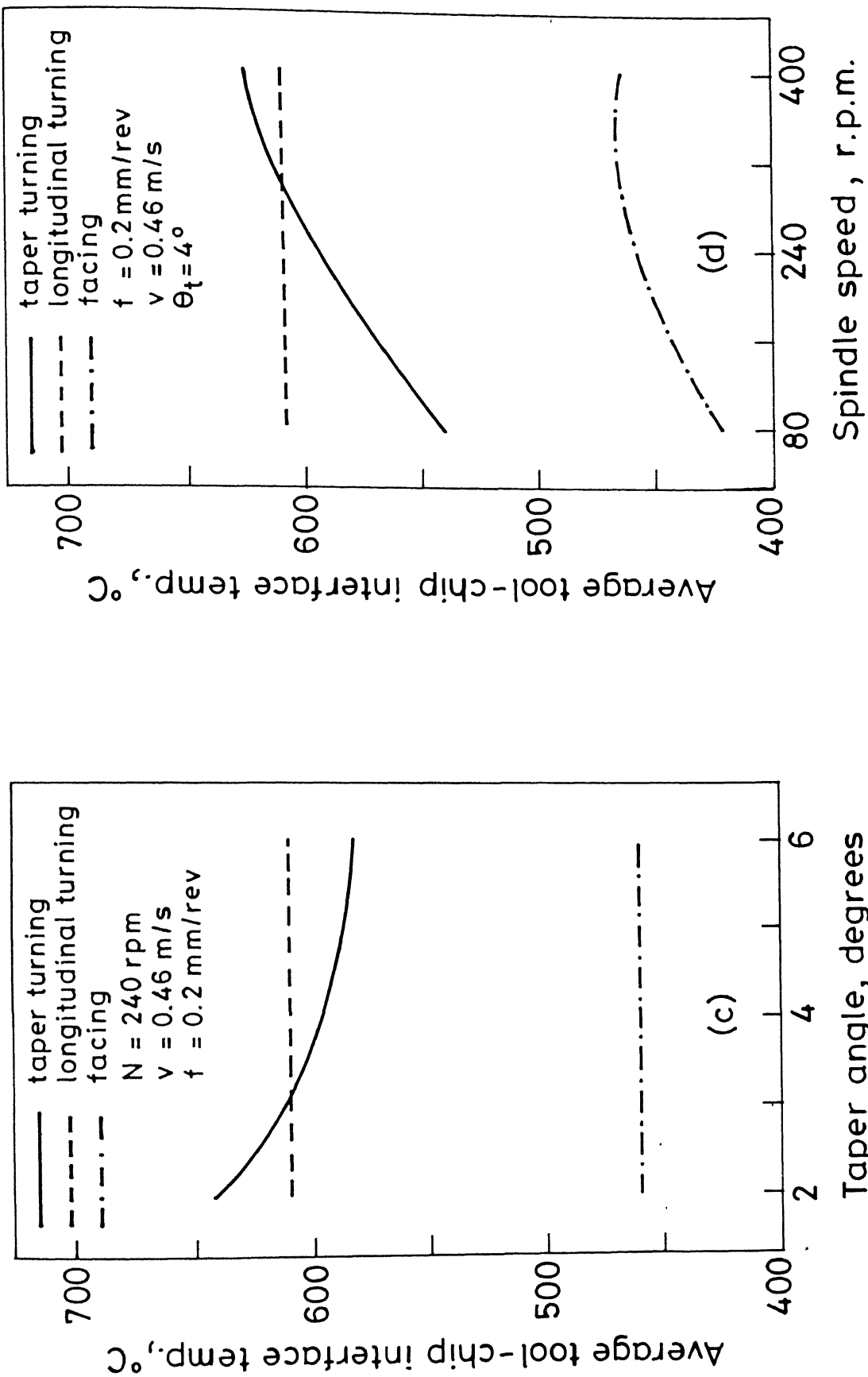


Fig. 5.5 Comparison of tool-chip interface temperature during longitudinal turning, taper turning and facing.

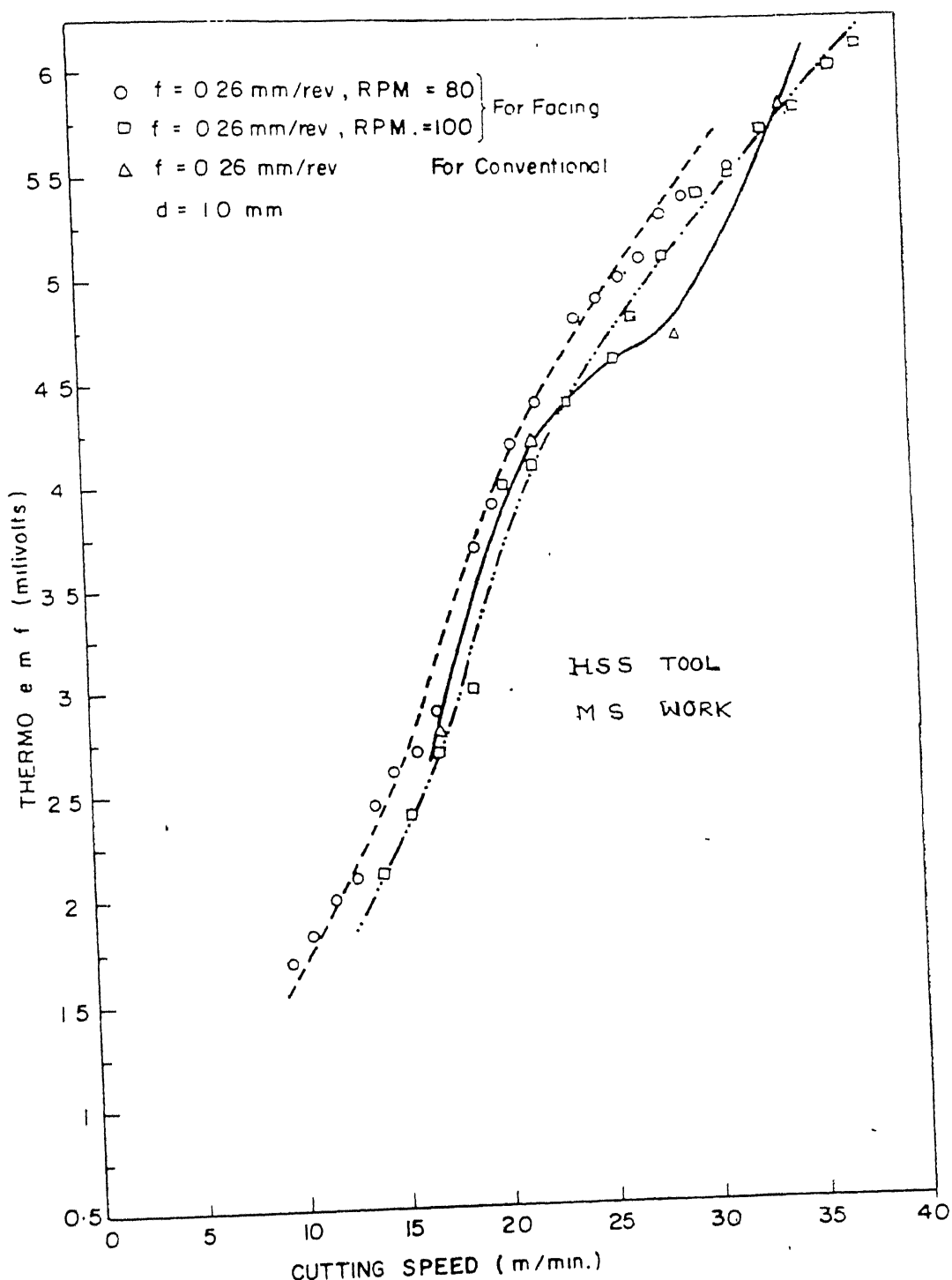


FIG. 56 a. CUTTING SPEED vs THERMO e.m.f. [REF. 12]

WORK MATERIAL : CAST IRON
TOOL MATERIAL : H.S.S.

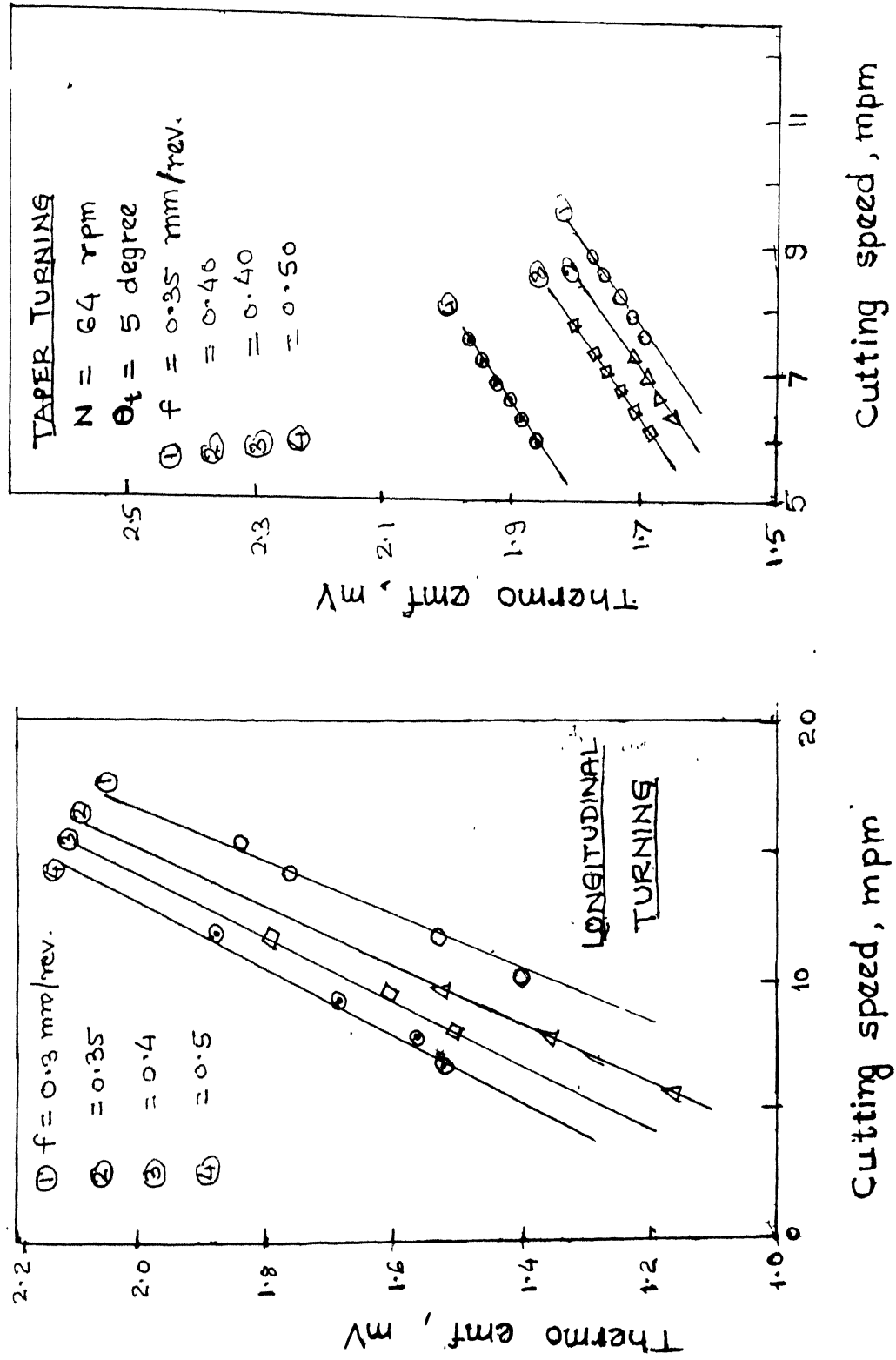


Fig 5.6 b. Variation of thermo e.m.f. (temperature) during longitudinal turning and taper turning. [Ref. 20].

CHAPTER 6

CONCLUSIONS AND SUGGESTIONS FOR FUTURE WORK

6.1 CONCLUSIONS:

From the results obtained in the present work, the following conclusions can be drawn:

- (1) Present model has been tested against analytical results for longitudinal turning and experimental results for longitudinal turning and facing test. It has been found that the correlation between the two is quite satisfactory.
- (2) It is observed that the pattern of variation of temperature, along rake and flank face of a tool during longitudinal turning, taper turning and facing is similar. Maximum temperature on the rake and flank face in all the three cases occurs at some distance away from the cutting edge.
- (3) It is also seen that mean tool-chip interface temperature is higher in case of longitudinal turning and lower in case of facing as compared to the temperature in taper turning for the same cutting conditions. Average tool-chip interface temperature in all the three cases are found to increase with the increase in cutting speed and feed rate. Increase in spindle speed results in an increase in average temperature in case of accelerated cutting. However, effects

of an increase in taper angle is to decrease the temperature in case of taper turning.

(4) From the above, it can be concluded that the average tool-chip interface temperature, as well as the local value of temperature at any location within the tool-chip-work system are not same during longitudinal turning, taper turning and facing operation under the same set of machining conditions.

6.2 SUGGESTIONS FOR FUTURE WORK:

(1) In the present analysis, the variation of physical properties (such as specific heat, density, thermal conductivity etc.) of tool and work materials with increase in temperature is not taken into account. This can be taken into to have better correlation with experimental results.

(2) Experiments may be conducted for a varieties of tool-work material combinations in a wide range of cutting conditions. Using these experimental results, the accuracy of the present model may be established.

(3) In the present analysis yield shear stress is assumed to be constant throughout in the PSDZ. In actual practice, it is not so. Hence a FE model can be developed which can take into account the variation in shear stress in PSDZ. This may yield more accurate results.

(4) Effects of temperature on microhardness of chips, coefficient of friction along rake face, strain rate and strain acceleration should be studied in depth.

REFERENCES

- (1) G. Lorenz, "The Economical Importance of Machinability Testing and Some Rapid Test Methods". *Metals, Australia*, Vol. 1, No.5, pp. 176-184, June 1969.
- (2) W.B. Heginbotham and P.C. Pandey, "Taper Turning Tests Produce Reliable Tool Wear Equations". 8th Int. MTDR Conf., Univ. of Birmingham, Sept. 1966, Pergamon Press Oxford, New York 1967.
- (3) V.K. Jain and P.C. Pandey, "Strain Acceleration: A New Concept in Metal Cutting and Its Effects on Accelerated Machinability Test". *Int. J. Engg. Prod.* 3(1), 1979, pp. 15-26.
- (4) M.C. Shaw, "Metal Cutting Principles", Oxford & IBM Publishing Co., New Delhi, 1969.
- (5) N.N. Zorev, "Metal Cutting Mechanics", Pergamon Press, Oxford, 1966.
- (6) J.H. Weiner, "Theoretical Estimation of the Shear Plane Temperature", *Trans. ASME*, Vol. 73, pp. 1331-1400, 1955.
- (7) A.C. Rapier, "Theoretical Investigation of the Temperature Distribution in the Metal Cutting Process", *Brit. J. Appl. Phys.* Vol. 5, pp. 400-412, 1955.
- (8) A.O. Tay, M.G. Stevenson, G. De Vahl Davis and P.L.B. Oxley, "A Numerical Method for Calculating Temperature Distributions in Machining from Force and Shear Angle Measurements". *Int. J. Mach. Tool. Des. Res.* Vol. 16, pp. 335-349.
- (9) P.D. Murarka, G. Barrow and S. Hinduja, "Influence of the Process Variables on the Temperature Distribution in Orthogonal Machining Using the Finite Element Method". *Int. J. of Mech. Sc.* Vol. 21, pp. 445-456. Pergamon Press Ltd. 1979.
- (10) M.G. Stevenson, P.K. Wright, J.G. Chow, "Further Developments in Applying the Finite Element Method to the Calculation of Temperature Distributions in Machining and Comparisons with Experiments". *Journal of Engineering for Industry, Trans. of ASME*, August 1983, Vol. 105, pp. 149-154.
- (11) H.S. Balaji, "An Application of FEM to the Estimation of Temperature Field in Machining with Coated Carbide Tools". M. Tech. Thesis, IIT Kanpur, July 1986.

- (12) V.K. Jain, "Facing Test for Machinability Testing", M.E. Dissertation, Univ. of Roorkee, July 1973.
- (13) V.K. Jain and P.C. Pandey, "Tool Wear Under Accelerated Conditions". Proc. of Int. Conf. on Wear of Materials, San Francisco, S.A., March 30-April 1, 1981, ASME, New York, 1981, pp. 447-455.
- (14) D. Kececiogulu, "Shear Strain Rate in Metal Cutting and Its Effects on Shear Flow Stress". Trans. ASME, 1958, 80, p. 158.
- (15) H. Ernst and M.E. Merchant, "Chip Formation, Friction and High Quality Machined Surface", Trans. ASME, Vol. 29, Series B, 1941, p. 299.
- (16) V.K. Jain and P.C. Pandey, "An Analytical Approach to the Determination of Mean Width of PSDZ in Orthogonal Machining". Proc. 4th Int. Conf. Prod. Engg., Tokyo, 1980, p. 434.
- (17) B.K. Gupta, "Investigations into Shear Flow Stresses during Accelerated Cutting". M.Tech. Thesis, IIT Kanpur, 1985.
- (18) S.S. Rao, "Finite Element Methods in Engg." Pergamon Press, 1985.
- (19) S. Kumar, "Investigations into Microhardness of Chips during Accelerated Cutting". M.Tech. Thesis, IIT Kanpur, Jan. 1987.
- (20) A.P. Singh, "Temperature Variation during Taper Turning of Cast Iron at Low Cutting Speed", M.E. Thesis, The Faculty of Engg., Univ. of Allahabad, 1976.

APPENDIX I

EXPERIMENTAL DATA

To test the validity of the analytical model developed in this text, experimental results have been borrowed from the work of Gupta [17], Jain [12] and Murarka [9].

Using the experimental results, response surface models for shear angle, cutting force, feed force and shear flow stress were developed by Gupta [17]. These models have been used to conduct parametric study given in Chapter 5.

Jain [12] has reported the results of cutting force and average tool-chip interface temperature during longitudinal turning and facing. The tool and work materials and the machining conditions in case of Gupta [17] and Jain [12] were almost same except the depth of cut.

Temperature results in reference [12] is in terms of mV of e.m.f., which has been converted into degree centigrade using calibration chart (Fig. A1), taken from the reference [4]. Experiments were conducted with d.o.c. as 1 mm. Due to unavailability of shear angle and feed force data [12], assumptions are made that the coefficient of friction (μ) and shear angle (ϕ) remain the same for d.o.c. as 0.6 mm [17] and d.o.c. as 1.0 mm [12]. Required data for 0.6 mm d.o.c. case are taken from ref.[17].

DESIGN OF EXPERIMENTS

The design of experiment is the procedure of selecting the number of trials and conditions for running them. Number of trials should be sufficient for solving the problem that has been set with required precision. The important features are, minimum total number of trials, simultaneous variations in all the parameters and the selection of clear cut strategy, permitting the investigator to make substantial decisions after each series of trials.

To determine the linear, higher order and interaction effects of different parameters on shear angle, shearflow stress, cutting and feed force, experiments were conducted for the trials shown in Tables A1, A2 and A3. The responses were measured or calculated and are given in Tables (A4, A5, A6)*. The second order response surface equation was fitted in the form

$$Y = B_0 + \sum_{i=1}^n B_i X_i + \sum_{i=1}^n B_{ii} X_i^2 + \sum_{i < j} B_{ij} X_i Y_j \quad (A.1.1)$$

where the values of B's are given in Table (A7) for temperature response. The labelled values of X_i 's are not used here (i.e. for temperature).

* Temperature response included in the table is obtained using present finite element model.

LEVELS FOR DIFFERENT FACTORS

TABLE A1 : Longitudinal Turning

Factors	Levels				
	-2	-1	0	1	2
Feed X_1 (mm/rev.)	0.10	0.15	0.20	0.25	0.30
Cutting X_2 Speed (m/s)	0.34	0.40	0.46	0.52	0.58

* Calculated values which were not available in the M/c Tool.

TABLE A2 : Taper Turning

Factors	Levels	-2	-1	0	1	2
Spindle Speed (R.P.M.) X_1		80	160	(240)*250	320	400
Taper Angle (Degrees) X_2		2°	3°	4°	5°	6°
Feed X_3 (mm/rev)		0.1	0.15	0.2	0.25	0.3
Cutting X_4 Speed (m/s)		0.34	0.4	0.46	0.52	0.58

* Calculated values which were not available in the m/c tool.

TABLE A3 : Facing

Factors	Levels				
	-2	-1	0	1	2
Spindle Speed (R.P.M.) x_1	80	160	(240)*250	320	400
Feed x_2 (mm/rev)	0.1	0.15	0.2	(0.25)* 0.26	0.3
Cutting Speed (m/s) x_3	0.34	0.4	0.46	0.52	0.58

*

Calculated values which were not available in the m/c tool.

PLAN OF EXPERIMENTS

TABLE A4 : Central Composite Rotatable Design with Half-Replicate
(CONVENTIONAL TURNING)

Sl. No.	Order	Feed rate mm.rev ⁻¹ (X_1)	Cutting speed ms ⁻¹ (X_2)	Shear angle -degrees	Shear flow stress kg mm ⁻²	F_C	F_T	$T_{av.}$
1.	9	0.15	0.40	20.02	49.67	20.00	16.75	603
2.	10	0.25	0.40	28.20	53.10	30.25	20.75	629
3.	11	0.15	0.52	19.58	53.72	21.00	16.00	713
4.	12	0.25	0.52	28.08	53.19	31.75	23.50	711
5.	1	0.10	0.46	18.37	49.50	13.25	10.00	688
6.	2	0.30	0.46	32.73	52.12	35.25	22.75	677
7.	13	0.20	0.34	21.42	50.82	25.00	18.00	536
8.	8	0.20	0.58	22.50	60.47	28.60	19.50	795
9.	3	0.20	0.46	22.22	51.47	25.00	18.00	623
10.	4	0.20	0.46	21.08	54.50	27.00	19.50	-
11.	5	0.20	0.46	22.57	51.73	25.00	13.00	-
12.	6	0.20	0.46	21.40	54.80	27.00	19.50	653
13.	7	0.20	0.46	21.53	50.99	24.50	16.75	-

TABLE A5 : Central Composite Rotatable Design with Half Replicate
(TAPER TURNING)

Sl. No.	Order	FACTORS				RESPONSES				T _{av}
		X ₁	X ₂	X ₃	X ₄	φ	σ	F _C	F _T	
1.	8	160	3°	0.15	0.40	23.75	41.70	8.25	14.00	279.89
2.	29	320	3°	0.15	0.40	23.88	56.40	18.25	12.50	308.00
3.	6	160	5°	0.15	0.40	24.67	28.45	15.25	18.50	331.28
4.	27	320	5°	0.15	0.40	24.30	46.28	16.75	12.50	291.09
5.	9	160	3°	0.25	0.40	28.10	44.20	28.50	23.50	419.90
6.	30	320	3°	0.25	0.40	28.55	44.46	25.00	16.75	341.61
7.	7	160	5°	0.25	0.40	30.40	70.10	38.75	25.00	518.36
8.	28	320	5°	0.25	0.40	26.88	42.70	25.00	18.00	343.19
9°.	5	160	3°	0.15	0.52	23.18	38.50	16.75	16.75	359.52
10.	26	320	3°	0.15	0.52	23.22	66.97	25.00	90.50	1400.45
11.	3	160	5°	0.15	0.52	20.93	54.30	20.00	14.00	342.42
12.	22	320	5°	0.15	0.52	25.92	62.26	23.00	18.00	452.54
13.	4	160	3°	0.25	0.52	26.70	36.63	23.50	19.50	382.49
14.	25	320	3°	0.25	0.52	27.55	63.03	36.75	26.25	547.77
15.	2	160	5°	0.25	0.52	27.03	53.20	35.25	30.50	576.21
16.	23	320	5°	0.25	0.52	25.72	49.80	28.50	19.50	411.09
17.	1	80	4°	0.20	0.46	24.97	38.70	18.50	20.75	383.15
*18.	31	400	4°	0.20	0.46	24.83	49.30	22.00	14.00	327.27
*19.	21	250	2°	0.20	0.46	27.02	59.20	20.00	27.75	522.43
20.	10	250	6°	0.20	0.46	31.35	49.24	20.00	11.00	310.77

TABLE A5 (Continued): :::::

TABLE A5 (Continued):

Sl. No.	Order No.	FACTORS				RESPONSES			
		X_1	X_2	X_3	X_4	\emptyset	F_C	F_T	T_{av}
21.	11	250	4 ^o	0.10	0.46	25.67	54.93	13.25	10.00
22.	12	250	4 ^o	0.30	0.46	29.32	45.86	31.00	20.75
23.	24	250	4 ^o	0.20	0.34	26.77	55.47	25.00	16.75
24.	13	250	4 ^o	0.20	0.58	25.50	84.36	36.75	22.25
25.	14	250	4 ^o	0.20	0.46	26.55	50.40	23.50	16.75
26.	15	250	4 ^o	0.20	0.46	26.65	52.93	23.50	15.25
27.	16	250	4 ^o	0.20	0.46	27.90	57.50	27.00	19.50
28.	17	250	4 ^o	0.20	0.46	31.22	49.90	22.00	14.00
29.	18	250	4 ^o	0.20	0.46	31.28	70.84	31.00	19.50
30.	19	250	4 ^o	0.20	0.46	33.73	50.30	23.25	15.25
31.	20	250	4 ^o	0.20	0.46	27.63	55.58	25.00	16.75

TABLE A6 : Central Composite Rotatable Design with Half Replicate
(Facing)

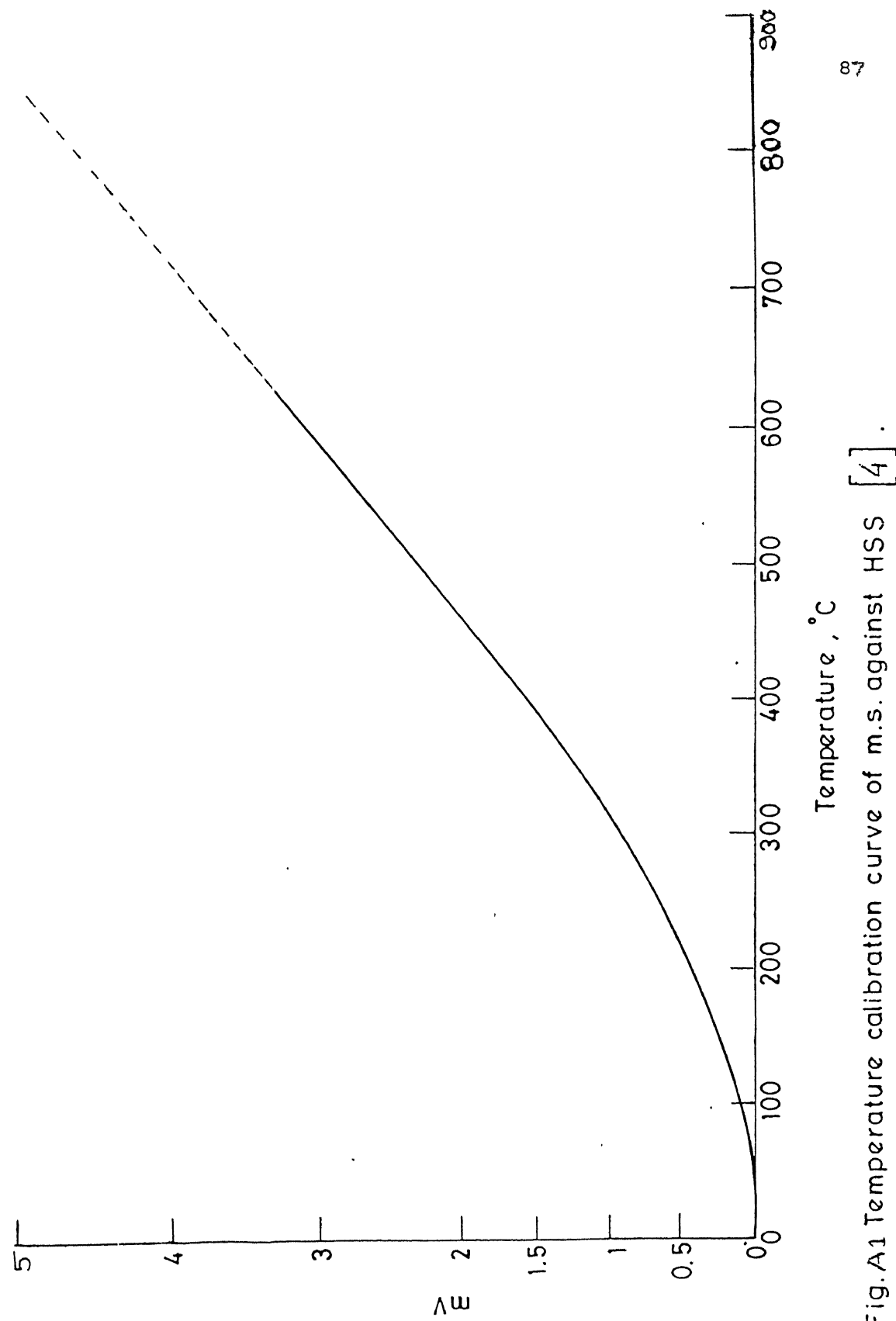
Sl. No.	Order	FACTOR			RESPONSES			
		X_1	X_2	X_3	ϕ	F_c	F_t	T_{av}
1.	16	160	0.15	0.40	25.60	72.77	23.50	14.00
2.	2	320	0.15	0.40	25.07	61.70	13.27	8.75
3.	17	160	0.26	0.40	26.99	70.23	35.25	18.00
4.	3	320	0.26	0.40	26.17	78.02	40.50	22.25
5.	18	160	0.15	0.52	27.30	57.84	20.00	14.00
6.	5	320	0.15	0.52	24.83	38.00	13.25	8.75
7.	19	160	0.26	0.52	37.98	53.40	31.75	90.50
8.	6	320	0.26	0.52	26.10	44.00	16.75	9.00
9.	20	80	0.20	0.46	28.93	68.00	27.00	14.00
10.	1	400	0.20	0.46	21.80	95.60	42.25	22.50
11.	7	250	0.10	0.46	27.83	60.00	13.00	9.50
12.	8	250	0.30	0.46	26.16	71.38	44.00	23.50
13.	4	250	0.20	0.34	25.15	63.60	27.00	15.25

TABLE A7 : Values of Constants in Response Surface Model
(Eqn. A.1.1) for Average Tool-Chip Interface Temperature

Constants	Longitudinal turning	Taper turning	Facing
B_0	██████████	-1529.3148	1660.1075
B_1	██████████	0.8214	12.7846
B_2	██████████	332.8345	-7820.2025
B_3	-	9981.9028	-10709.4900
B_4	-	-505.4196	-
B_{11}	██████████	- 0.0000	0.0057
B_{22}	██████████	14.4073	10249.8070
B_{33}	-	-503.5757	14535.1890
B_{44}	-	6857.3914	-
B_{12}	██████████	-1.1110	-21.2768
B_{13}	-	-21.2190	-25.8536
B_{14}	-	17.9569	-
B_{23}	-	1359.5124	22819.4630
B_{24}	-	-1085.9270	-
B_{34}	-	-21878.5380	-

* Levelled values of factors X_i 's in Eqn. (A.1.1) are not used.

These constants are valid only when direct values of X_i 's (for example $N=160$ r.p.m, etc.) are used in the response surface model eqn.



APPENDIX II

TABLE A8 : Physical Properties of Tool Work Materials Used

Material	Density ρ , kg/m ³	Specific heat C_p , watt-sec./kg-°C	Thermal conductivity K, watt/m-°C
H.S.S. (tool)	8700	433	26
M.S. (work)	7833	480	45

TABLE A9 : Constants of Power Law Equations in the Form $B = A N^{n_{11}} \Theta_t^{n_{12}} F_t^{n_{13}} V^{n_{14}}$

ϕ	Taper Turning			Facing		
	F_c	F_t	θ	τ	F_c	F_t
A	30.5395	250.346	559.4663	2233.0993	82.2896	411.4324
n_{11}	0.0141	0.2060	0.1884	- 0.0562	-0.1729	- 0.0206
n_{12}	0.056	0.0011	0.1974	- 0.5053	0	0
n_{13}	0.2352	0.0068	0.9725	0.4413	0.0626	0.1335
n_{14}	0.1418	0.6285	0.7826	1.013	0.1404	- 0.9470

Units : ϕ - degree, τ - N/mm², F_c - N, F_t - N.